Reducing the exposure dose of portable detectors with SiPM : Controlling X-ray Dose by Calculating Optimal Imaging Levels Implementation and evaluation

Byung Wuk Kang

The Graduate School
Yonsei University
Graduate Program of Biomedical Engineering

Reducing the exposure dose of portable detectors with SiPM : Controlling X-ray Dose by Calculating Optimal Imaging Levels Implementation and evaluation

A Dissertation
Submitted to the Graduate Program of Biomedical Engineering
and the Graduate School of Yonsei University
in partial fulfillment of the
requirements for the degree of
Doctor of Philosophy

Byung Wuk Kang

December 2023

This certifies that the dissertation of
Byung Wuk Kang is approved.

_____
Thesis Supervisor: Sun K. Yoo

_____
Thesis Committee Member: Jong-Chul Park

_____
Thesis Committee Member: Yong Oock Kim

_____
Thesis Committee Member: Yonghyeon Yun

_____
Thesis Committee Member: Byung-Chae Lee

The Graduate School
Yonsei University
December 2023

Acknowledgements

박사과정을 밟으면서 정말이지 수많은 분들의 도움과 가르침으로 본 논문을 완성할 수 있게 되어 무한한 감사의 말씀을 전합니다.

업무와 학업을 병행하면서 부족함이 있음에도 격려와 조언을 해주시며, 연구 방향을 이끌어주신 유선국 교수님께 깊은 감사를 드립니다. 교수님의 가르침을 통해 더욱 성장할 수 있었으며 앞으로도 현재에 안주하지 않고 배움을 갈구하는 자세를 지속하도록 하겠습니다. 부족한 논문임에도 바쁘신 와중에 심사를 진행해 주신 박종철 교수님, 김용욱 교수님, 윤용현 교수님, 이병채 교수님께 머리 숙여 감사드립니다.

연구 진행을 위한 서재정 대표님과 황강민 소장의 지원에 감사드립니다. 실험 환경의 지원이 없었다면 이 연구는 진행되기 어려웠을 것입니다. 본 연구의 핵심적인 역할을 해준 김인수에게 특별한 감사의 말을 전하며, 개인적으로 연구를 지원하고 도와준 김민규, 조미정, 김남형, 유광선, 김혜빈, 아이한 마메도프를 비롯한 팀원들과 저와 함께해온 모든 인원에게 감사의 마음을 전합니다.

2014년 석사부터 시작해 10년 동안 많은 추억을 남겨준 연구실 권준환, 오경택 박사, 이번에 같이 심사 받는 김병남, 권오윤, 박현목 학생과 다음 학기 논문을 준비하는 김상규 학생을 비롯한 모든 인원에게 앞으로도 좋은 일들만 가득하기를 바랍니다.

무엇보다 옆에서 가장 많은 응원을 해준 아내 주서희와 두 아들 동훈, 승훈에게 사랑의 마음을 전합니다. 그리고 한결같이 저를 믿어주시는 아버지, 어머니 그리고 장모님을 포함한 모든 가족에게 감사합니다.

많이 부족했음에도 한결같이 믿어주고 응원해 주시는 모든 분들로 인해 이 논문이 완성될 수 있었습니다. 감사합니다.

2023년 12월

강 병 욱 올림.

Table of Contents

List of Figures

List of Tables

Abstract

Reducing the exposure dose of portable detectors with SiPM: Controlling X-ray Dose by Calculating Optimal Imaging Levels Implementation and evaluation

Byung Wuk Kang
Graduate Program of Biomedical Engineering
The Graduate School Yonsei University

Due to their miniaturization and lightweight design, portable X-ray detectors have the advantage of being able to quickly approach a patient's location and acquire real-time images for rapid diagnosis, but this mobility poses a dose control challenge. This paper aims to present and evaluate a method to minimize patient radiation exposure by implementing optimal dose control using a compact SiPM sensor that can be embedded in a portable X-ray detector.

This study presents an imaging evaluation based on IEC 62220-1, an international standard for X-ray imaging devices, to determine the DQE of the detector and the dose that can have optimal image quality, and to match the output of the imaging ADU and SiPM sensor to control the optimal dose.

For the Skull AP, the experimental results showed a dose reduction of

approximately 57% from the manufacturer's reference dose of 342.8 μGy to the optimal controlled dose of 148.3 μGy. For the Chest AP, a dose reduction of 66% was observed with an optimal controlled dose of 27.9 μGy compared to the manufacturer's reference dose of 81.9 μGy. These results demonstrate that optimal dose control with SiPM sensors can significantly reduce patient radiation exposure.

X-ray dose management is a crucial topic in medical imaging. It is already practiced in advanced countries such as the United States and Europe. Research and interest in dose management for patients and medical staff are continuously increasing in Korea. Against this background, the experiments in this paper demonstrate that it is possible to control the dose for low patient exposure while maintaining optimal image quality using SiPM, which is expected to make an important contribution to radiation dose control and image quality improvement in the medical imaging field.

Key Words : X-ray exposure, optimal dose control, image quality, SiPM, portable detector

Chapter 1

Introduction

X-rays are one of the most used diagnostic devices in modern medicine and are rapidly growing in the medical field. X-rays are one of the essential tools for doctors to non-destructively observe and diagnose the inside of a patient. Traditionally used to identify ruptures, fractures, and deformities, high-resolution X-ray imaging now allows for detailed visualization of the microscopic structure of tissues. This contributes to increased diagnostic accuracy and faster treatment options for patients[1].

Portable X-ray detectors are essential equipment in many situations where mobility and rapid on-site inspection and diagnostics are necessary. They occupy less space than stationary equipment and are especially useful in environments that require non-invasive testing and quick decision-making are required[2].

Due to their miniaturization and lightweight design, portable X-ray detectors can quickly access a patient's location and acquire real-time images, enabling doctors to quickly make a diagnosis. This is especially important in medical settings where a quick diagnosis is needed in an emergency or in industrial settings where structural inspections are required. Advances in wireless communication technology also allow data to be transmitted and shared in real time, improving the speed of decision-making. This includes mobile emergency medical systems that can deliver emergency medical diagnoses to the right place at the right time[3].

Portable X-ray detectors are widely used in the medical field as well as in industrial and security applications. In medicine, they are used for patient diagnosis in emergency rooms, operating rooms, and during transportation, and in

industry, they are applied in non-destructive testing applications such as metal flaw detection, quality control, and structural inspection[4]. As such, portable X-ray detectors play a significant role in modern healthcare and industry by providing mobility and rapid medical imaging. However, with mobility comes the challenge of dose control, so most portable detectors are now incorporating a small silicon photomultiplier (SiPM) sensor to detect X-ray irradiation conditions, implementing a feature called Automatic Exposure Detection(AED)[5]. The SiPM is a silicon photomultiplier tube that provides extremely high sensitivity and high energy resolution, even detecting single photons, but detectors are using the SiPM to simply determine the X-ray trigger.

Dose management is directly related to radiation exposure. While in the past it has only investigated for patient exposure, recent years have seen active studies on the exposure of radiation workers to medical radiation. Dose management has an important impact on the safety management of patients and workers[6]. The change in hardware equipment from the analog method of using a film-type receptor to the digital radiography (DR) method has provided a convenient environment for users to perform examinations and has the advantage of increasing image quality. In particular, with the introduction of the DR System method, it is possible to adjust the captured image to the appropriate range of density through the process of digitally correcting the radiation dose exposed during the examination. However, the convenience of adjusting images without compromising quality can result in excessive doses to patients, and users have been found to neglect dose and image quality management[7]. This is due to the fact that there is a transition from analog to digital imaging systems, but there are no guidelines for this. To date, there is still no consensus on parameter adjustments for X-ray irradiation conditions[8][9]. Research is therefore ongoing to minimize the effective dose to the patient, as described by the as low as

reasonably practicable (ALARP) principle, while providing high-quality images that allow for the best possible diagnosis[10][11].

Therefore, as a way to control the dose for optimal image acquisition while minimizing patient exposure, this paper aims to implement a method for measuring the optimal dose by applying a small-sized SiPM sensor inside a portable detector and evaluating its performance.

Chapter 2
Theoretical Background

2.1 X-ray

German physicist Wilhelm Conrad Roentgen discovered X-rays while testing a gas discharge in a sealed Crookes vacuum tube to prevent light from escaping. He noticed that fluorescent material outside the vacuum tube glowed, which he named 'X-beams', later known as X-rays. He later confirmed that X-rays could penetrate objects, revolutionizing many applications in the medical and scientific fields[12]. X-rays are generated by breaking radiation (bremsstrahlung), which accelerates electrons to high voltage and causes them to fall from a high energy state to a low energy state as they strike a metal plate. As the accelerated electron approaches the nucleus of an atom, its speed is reduced by the nucleus' coulomb's force. The decelerated electron deviates from its original orbit and releases the kinetic energy it had while decelerating as electromagnetic waves. This electromagnetic wave is called an X-ray[13].

2.1.1 X-ray tube

X-ray tubes that produce radiation were developed by William David Coolidge in 1913. His invention, the Coolidge Tube, uses a tungsten-catalyzed, high-speed rotating anode that can produce a stable, continuous stream of X-rays. This technology is still the most commonly used today.

Figure 1 shows the structure of an X-ray tube. To produce X-rays, an X-ray tube consists of a heat source that emits thermal electrons, a high voltage that accelerates the thermal electrons, a metal plate that collides with the accelerated thermal electrons to produce X-rays, and a vacuum tube that facilitates the production of X-rays. An X-ray tube consists of several components necessary to produce X-rays. These components include a heat source that emits thermal electrons, a high voltage that accelerates the thermal electrons, a metal plate where the accelerated thermal electrons collide to produce X-rays, and a high vacuum environment that facilitates the generation of X-rays. The X-ray tube consists of a cathode and an anode, which are enclosed in a vacuum tube that maintains a high vacuum of about 10^{-7} mmHg. This high-vacuum environment minimizes electron scattering and energy loss, and prevents oxidation and electrical arcing, improving the stability of the entire system. The cathode has a spiral filament structure that generates heat, while the anode is made of a metal such as tungsten. When the cathode is heated, electrons are released through heat dissipation, and due to the high voltage difference with the anode, these electrons are accelerated to the anode. As the accelerated electrons collide with the anode, X-rays are emitted. The greater the number of electrons colliding with the anode, the more x-rays are produced, so the intensity of the x-rays is proportional to the tube current. Also, the higher the voltage, the faster the electrons are accelerated, resulting in higher energy x-rays when they collide with the anode[14].

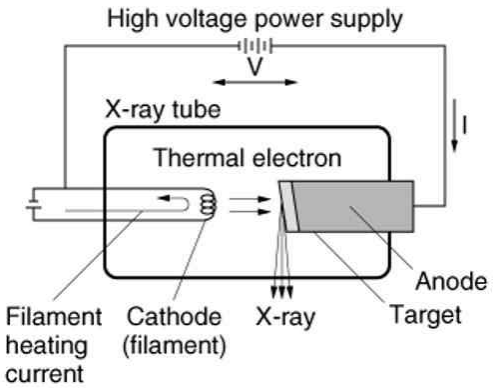

Figure 1. X-ray tube structure

Source: www.matsusada.com/application/ps/x-ray_tube/

Inside the vacuum tube, the kinetic energy of the electrons is increased by the high voltage applied to both ends of the X-ray tube when the thermal electrons generated by the filament, which is the negative electrode of the X-ray tube, change the voltage applied to both ends of the X-ray tube and the voltage of the X-ray tube increases[15]. Figure 2 is an image of an X-ray braking radiation. X-rays are generated by braking radiation (Bremsstrahlung), in which the kinetic energy of the electrons traveling at high speed is converted into electromagnetic waves by colliding with the metal plate, which is the anode electrode. The lost energy is emitted as X-rays in an amount proportional to the hv.

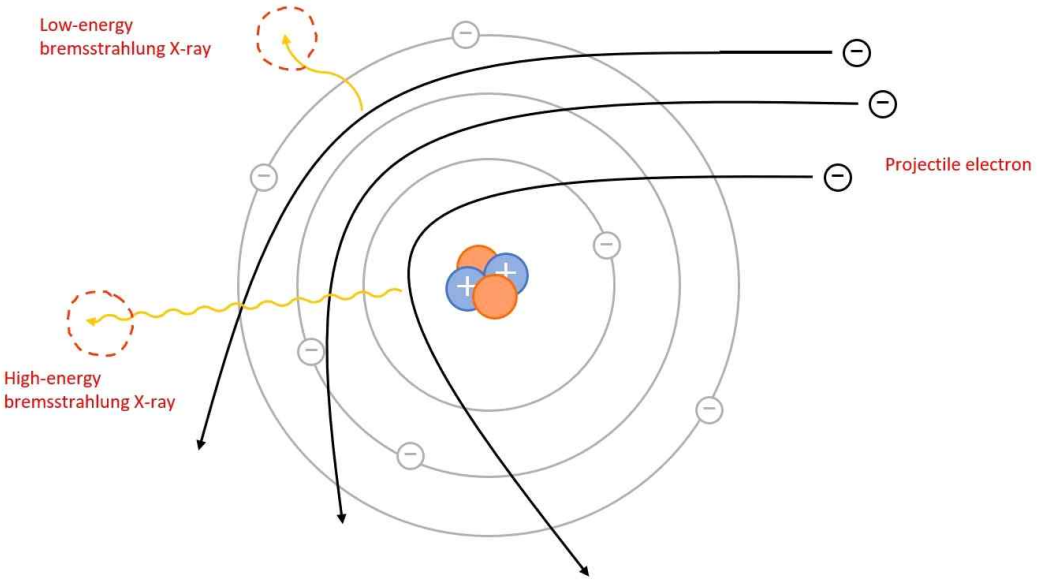

Figure 2. braking radiation

If all of the kinetic energy eV of a cathode ray electron is converted to the energy E of an X-ray photon by Duane-Hunt's Law, then it is equal to Equation (1). h is Planck's constant ($6.626 \times 10^{-34} Js$), v is the frequency of the X-ray photon, and c is the speed of light, which is the product of the wavelength (λ) and the frequency v.

$$E = hv = \frac{hc}{\lambda} = eV \tag{1}$$

e is the charge on the electron and V is the accelerating voltage. Since the charge e is constant, the energy E is proportional to V and the wavelength lambda is inversely proportional to V.

2.1.2 Tube Voltage and Tube Current

The tube voltage is measured in kV and the value is expressed as the peak value of the alternating current. If the supply voltage is high, the speed of electron movement increases, which increases the intensity of the generated X-rays, which increases the transmittance. X-ray intensity (total energy of X-rays per unit time) I is proportional to the square of the Tube voltage V.

The tube current is the current flowing in one direction from the anode to the cathode of the X-ray tube. The higher the X-ray tube current, the more electrons are emitted.

As the number increases, the X-ray dose increases. If the tube voltage and exposure time are the same, the X-ray intensity I is proportional to the tube current i.

The X-ray quality depends on the tube voltage, and the X-ray dose depends on the tube voltage and tube current. The higher the tube voltage and tube current, the higher the average energy of the X-ray photons. The X-ray dose Q in Equation (2) is proportional to the square of the supply voltage V, the supply current i, and the irradiation time t. Where Z is the atomic number and k is the proportionality constant[16].

$$Q = kiZV^2t \tag{2}$$

Digital radiography represents an important development in the field of radiology and is rapidly replacing the traditional analog film screen method. A key advantage of this technology is the digitization of images, which allows for higher image quality and more efficient data management. However, digital radiology suffers from a relatively high radiation dose to the patient[17]. This is due to the

trade-off between image quality and radiation dose, so optimization to minimize patient radiation exposure while maintaining image quality for accurate diagnosis is essential. Radiation has a high energy state and can cause damage to the human body, which we define as 'exposure'. The unit used to measure the effect of radiation on the human body is the sievert (Sv), but this is generally too large a unit, so smaller units such as the millisievert (mSv) or microsievert (μSv) are commonly used. Naturally, humans are exposed to trace amounts of radiation from the environment and even from potassium and carbon in the body. The majority of ionizing radiation exposure to the general population is from natural sources[18]. In pediatric radiology in particular, optimization is even more important due to the higher risk of late radiation effects [19]. This is due to the sensitive tissues of young patients and the potential radiation effects over a longer life span.

Selecting the appropriate radiation quality is a key part of optimization[20]. The low-energy portion of the X-ray spectrum increases the patient dose without directly affecting image quality. Therefore, methods are utilized to reduce the low-energy portion and increase the effective energy of the beam by increasing the kVp (kilovolt peak) or by hardening the X-rays through additional filtration. This can reduce the contrast of the image, but the image contrast can be restored through the use of digital detectors and appropriate post-processing[21].

2.2 Flat Panel Detector

Flat panel detectors (FPDs) are used in many applications, including medical and industrial, including portable detectors, and their typical internal structure is shown in Figure 3. At the top of the FPD is the scintillator, which converts X-rays into visible light. The scintillator accepts X-rays and converts them to visible light, which is the first step in image formation. The efficiency and conversion capabilities of the scintillator directly affect the quality of the image. Immediately below the scintillator is the Thin Film Transistor (TFT) panel. The TFT panel is responsible for converting the visible light from the scintillator into electrical signals. This electrical signal is then converted into digital data. The performance of the TFT panel has a significant impact on the resolution, contrast, and signal-to-noise ratio of the image. The middle part of the FPD uses a plate to hold the panel steady. This plate is typically made of a lightweight yet durable material such as magnesium or aluminum. This choice of material is important to improve the durability and mobility of the FPD. Especially for portable detectors, lightweight contributes to user comfort and patient accessibility.

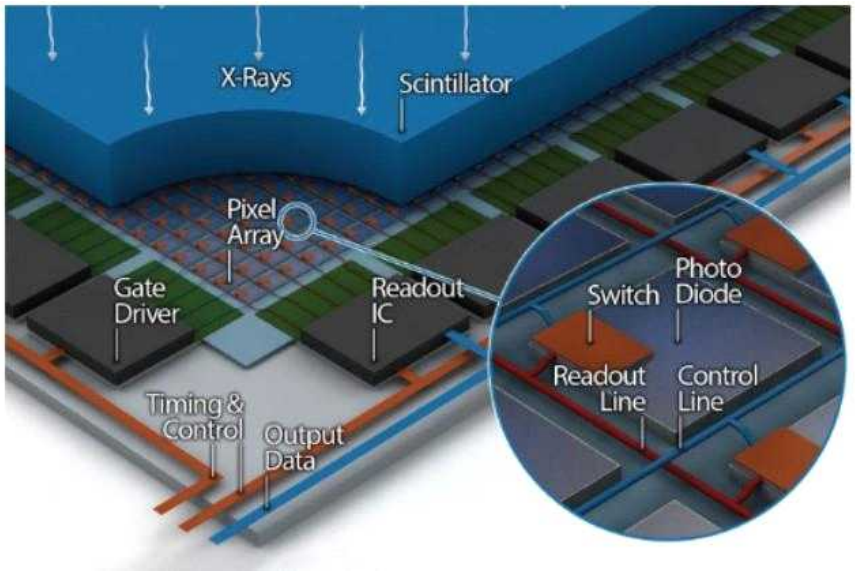

Figure 3. Flat Panel Detector Structure

Source: wellmanxray.com/blog/everything-you-need-to-know-about-flat-panel-detector/

The scintillator generates photons in proportion to the X-rays, and the photodiode electrodes of the TFT array generate a corresponding charge on the capacitor in proportion to the photons. A gate, ROIC control circuit scans the stored charge of each pixel and converts it into a digital signal. Scintillators use gadolinium oxide (Gd2O2S) or cesium iodide (CsI). CsI is a columnar phosphor that has the advantage of better resolution and absorption efficiency than Gd2O2S, which is an amorphous phosphor.

In Figure 4, a scintillator is a material that accepts X-rays and converts them into photons (visible light). These photons are detected by the photodiode electrodes of the TFT array, and in the process, charge is accumulated in a capacitor[22]. This accumulated charge is then scanned at each pixel through a gate and readout integrated circuit (ROIC) control circuit and converted into a digital signal[23]. This process converts the X-ray image into digital data that is

then processed by a computer system.

The type of scintillator has a direct impact on image quality. The most commonly used scintillator materials are gadolinium oxide (Gd2O2S) and cesium iodide (CsI). While Gd2O2S is widely used as an amorphous phosphor, CsI is a columnar phosphor that has excellent advantages in resolution and absorption efficiency. CsI scintillators can convert X-rays into visible light more efficiently, resulting in sharper images. However, CsI also has disadvantages such as high cost, complexity of the deposition process, and physical fragility[24].

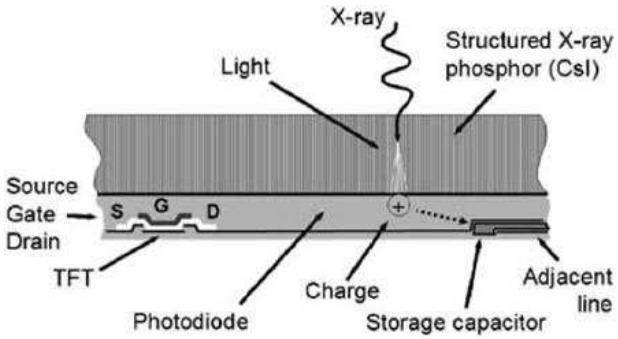

Figure 4. Method of X-ray Conversion to Digital in FPD

Source: A Novel Sub-Pixel-Shift-Based High-Resolution X-ray Flat Panel Detector(2022)

2.3 SiPM Sensor

A silicon photomultiplier (SiPM) is a highly sensitive photomultiplication sensor. The key feature of this device is that the level of the output signal depends on the bias voltage. Since a higher bias voltage can generate a larger output signal, SiPM typically uses a high input voltage[25].

Figure 5 shows the structure of SiPM, which comprises an array of numerous small photodiodes. Each photodiode is responsible for detecting microscopic photons. These microcells are connected in parallel, resulting in a high dynamic range that can detect photons from a single photon to thousands of photons in a device with a square millimeter area. This enables SiPMs to provide highly sensitive and precise light detection[26].

Small SiPM are typically 10 × 10 mm or less. SiPMs can be used in combination with scintillators, which can further improve the photodetection efficiency depending on the type of scintillator. In addition, SiPM has the property of insensitivity to magnetic fields, so it can be used in strong magnetic field environments such as magnetic resonance imaging(MRI)[27]. In the medical imaging field, these features have led to the use of SiPM in high-precision imaging equipment such as positron emission tomography (PET) scanners.

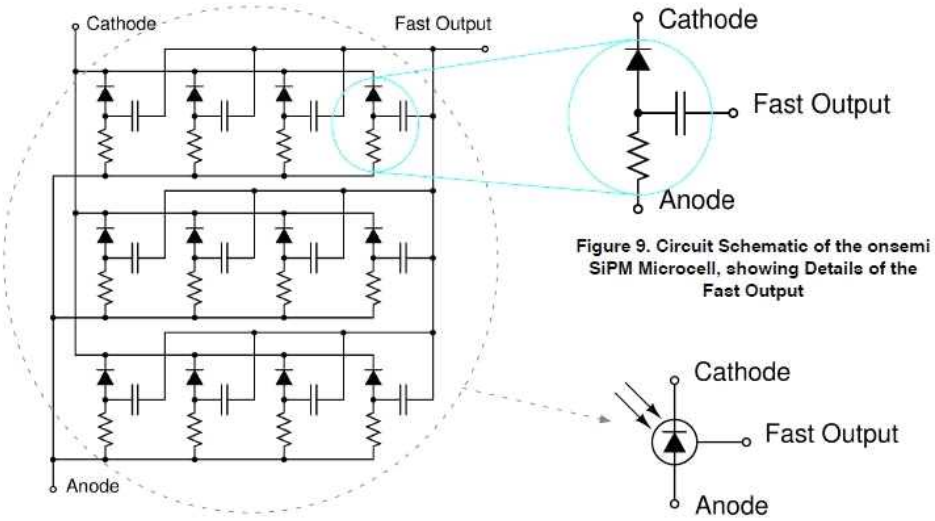

Figure 5. Structure of SiPM Sensor

Source: The detection efficiency study of NaI(Tl) scintillation detector with the different numbers of SiPMs(2022)

2.4 Dosimeter

Figure 6 shows different types of dosimeters. Film Badge, Thermo luminescent Dosimeter (TLD), Ionization Chamber, etc. are commonly used for radiation dose measurement and each has its advantages and disadvantages[28][29].

Film Badge: Film Badge is a method of detecting radiation exposure through discoloration of the film. This method is cost-effective and has the advantage of providing a visual analysis of the type and amount of radiation. However, Film Badges are disposable and may have limited accuracy for long-term exposure. It also has the disadvantage that results can be affected by environmental conditions[30].

Thermo Luminescent Dosimeter (TLD): TLDs measure radiation exposure by utilizing the property of emitting light when heat is applied. TLDs can be used repeatedly and provide accurate measurements at various energy levels. They also provide stable performance, but require specific equipment to read the measured data and cannot provide immediate results. TLDs are particularly useful in the medical field for precise monitoring of patient radiation exposure[31].

Ionization Chamber: Ionization chambers determine radiation dose by measuring the ions produced by radiation. This method is highly accurate, provides immediate results, and can be used repeatedly. However, ionization chambers are relatively large and heavy, and can be affected by the temperature and humidity of the surrounding environment[32][33]. Because of these characteristics, ionization chambers are primarily suitable for radiation measurements in internal environments, such as hospitals, or in fixed locations.

(a) (b) (c)

Figure 6. Dosimeter types (a) Film badge (b) TLD (c) Ionization Chamber

2.5 Image quality valuation

Evaluating the image quality of an X-ray detector is primarily based on three key factors: Noise, Resolution, and Contrast. The interaction of these three factors determines the image characteristics, as shown in Figure 7. Measures such as Signal-to-Noise Ratio (SNR), Noise Power Spectrum (NPS), and Modulation Transfer Function (MTF) are used to evaluate the sharpness and noise level of an image[34]. SNR is the signal-to-noise ratio, NPS is the frequency distribution of the noise, and MTF is the resolution of the system. Collectively, these metrics are analyzed to evaluate image quality through Detector Quantum Efficiency(DQE)[35]. In other words, DQE is a holistic indicator of x-ray image quality. DQE is an indicator of how efficiently the detector converts x-rays into images, with higher DQE values indicating better image quality.

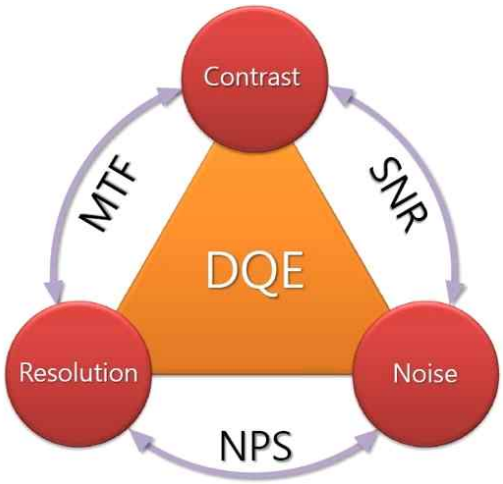

Figure 7. Key elements of image quality

2.5.1 Signal-to-noise ratio (SNR)

SNR is an important metric in medical imaging, representing the ratio of the signal level to the noise level. The signal is the important part of the image that provides useful diagnostic information, while noise is the random variation in the image that is not part of the true image. Noise can come from a variety of sources, including electronic noise in the detector, quantum noise in X-ray photon detection, and artifacts in the imaging process[36]. A high SNR means less noise and a stronger signal, which improves image clarity and diagnostic accuracy. Conversely, a low SNR reduces the usefulness of the image and can affect the accuracy of the diagnosis. Therefore, SNR is used as an important indicator to evaluate the image quality[37].

To distinguish between the two materials, you need a good contrast between them. As Figure 8, given the same SNR, the higher the contrast value, the better the two materials can be distinguished. Increasing contrast helps to improve image quality[38]. In medical imaging, image contrast can be improved by increasing the radiation dose, but this involves a tradeoff of increased radiation exposure to the patient. In such situations, It is then important to reduce the radiation dose while maintaining image quality.

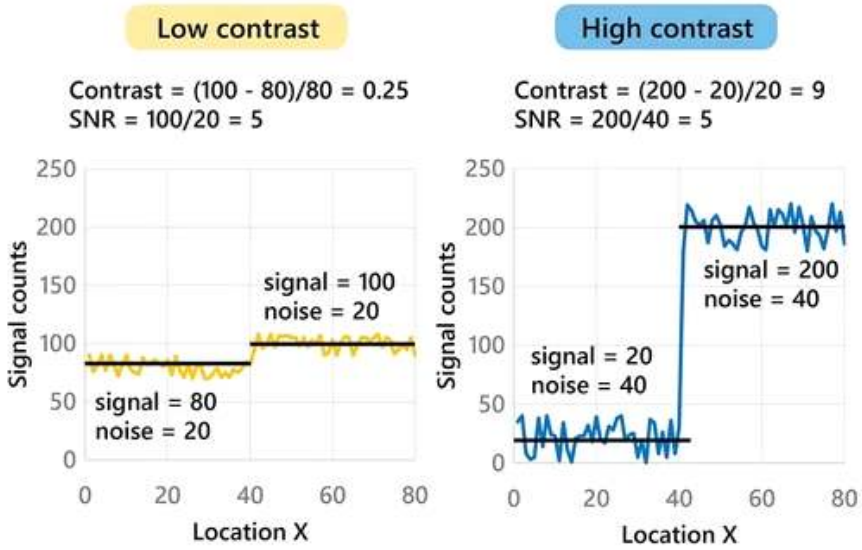

Figure 8. Signal impact as a function of contrast intensity

Source: imaging.rigaku.com/blog/how-improve-signal-noise-ration-xray-ct-images

2.5.2 Noise power spectrum noise power spectrum (NPS)

In video, noise is typically quantified using statistical measures such as variance or standard deviation. These measures indicate the extent to which signal variation in the input image has been modified by the system. In imaging systems in particular, noise of the same magnitude has a greater impact when the object is smaller, making it harder to distinguish visually. For this reason, noise should be measured and evaluated through a metric that is combined with spatial resolution, which is called NPS[39].

This metric, also called NPS, or Wiener Spectrum, is a way to interpret the noise variation in an image as a function of frequency[40]. It quantifies the distribution of signal or image noise at different frequencies, which is important for understanding the effect of noise on images at different spatial resolutions. NPS helps evaluate the noise characteristics of an imaging system, playing a crucial role in optimizing image quality and diagnostic accuracy[41].

NPS is a function of spatial frequency, which has the advantage of allowing noise to be evaluated by subdividing it into spatial frequency regions. This property is particularly useful when evaluating noise characteristics in digital X-ray images. Therefore, NPS analysis is an essential tool for managing noise and improving image quality in medical imaging.

2.5.3 Modulation Transfer Function (MTF)

MTF is an important quantitative factor in X-ray imaging that describes the difference in contrast with frequency of an incoming object. It represents the output delivery characteristics of the system for an input frequency signal and is used to determine the resolution and sharpness of the image in the frequency domain. MTF indicates how well the contrast of the object being photographed is transferred to the final image and is defined as the spatial frequency response of the system. It is a curve that shows the contrast achieved at different spatial frequencies, with higher frequencies representing finer detail. In general, MTF tends to decrease at higher frequencies.

As shown in Figure 9, the MTF is a curve graphed in frequency space, which is obtained by Fourier transforming the line spread function (LSF) or point spread function (PSF). One of the MTF measurement methods is the Edge Method, which uses a phantom made of tungsten or lead with high X-ray absorption to obtain the LSF through the derivative of the image taken at an angle of about 1.5° to 3.0° to the pixel array, and then Fourier transforms it to obtain the MTF. This method is currently specified in the International Electrotechnical Commission (IEC) 62220-1 standard as the MTF measurement method for digital X-ray imaging devices. [42][43]

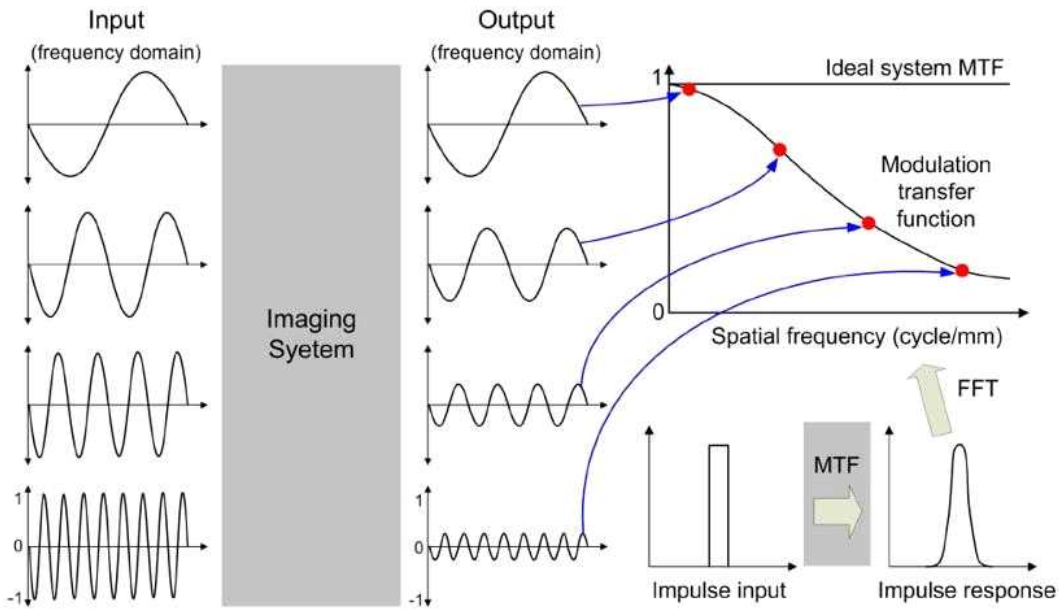

Figure 9. Frequency space versus MTF graph

Source: https://slideplayer.com/slide/9698277

2.5.4 Detective Quantum Efficiency (DQE)

The efficiency of an X-ray imaging system can be evaluated by its DQE. DQE is a measure of how much information is converted into an image relative to the input X-ray energy. A high DQE means that a high quality image can be obtained with a low radiation dose. Figure 10 shows the correlation between MTF and NPS for calculating DQE as described earlier.

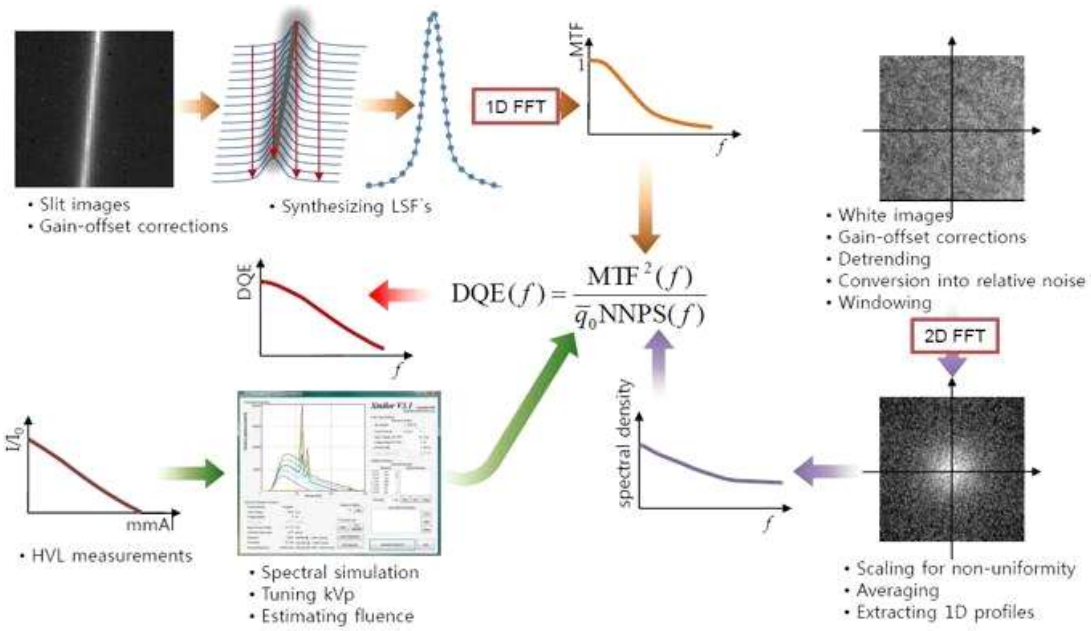

Figure. 10 Correlation between DQE, MTF, and NPS

Source: https://slideplayer.com/slide/9698277

The K_a value in Equation (3) is a measurement of the dose (μGy) absorbed in free air in the image plane using a solid-state detector dosimeter, obtained after calibration to the dosimeter-detector. It is an important metric for evaluating the

dose efficiency of an X-ray imaging system.

$$DQE = \frac{SNRout^2}{SNRin^2} = \frac{(G \cdot MTF)^2}{NPS \cdot K_a \cdot SNRin^2} \quad (3)$$

$SNRin^2$ values are based on standardized spectra according to the International Electrotechnical Commission's IEC 62220-1 standard in Table 1, which represents the SNR of an image[44]. NPS is the noise power spectrum measured at the same air kerma. The G value is the gain of the detector at zero spatial frequency, which indicates how efficiently the detector converts the X-ray signal into an electrical signal[45]. Air kerma is measured a certain distance away from the detector surface to minimize X-ray scattering. The importance of this measurement lies in the fact that the exposure at the detector surface is determined by the inverse square law. These measurements are essential for evaluating the performance and image quality of an X-ray detector, which allows for an accurate assessment of the detector's efficiency, image sharpness, and overall imaging system performance. These evaluations play significant role in improving the quality of medical imaging and increasing the accuracy of diagnosis.

Table 1. IEC 62220-1 RQA

Spectrum	Added filtration [mmAl]	HVL [mmAl]	$SNRin^2$ [#/(mm^{2}μGy)]
RQA3	10	4.0	21.76
RQA5	21	7.1	30.17
RQA7	30	9.1	32.36
RQA9	40	11.5	31.08

2.6 Automatic exposure detection (AED)

AED was first developed by NMI, and most newer detectors have built-in AED functionality. The AED is operated in the form shown in Figure 11. AED is a feature that enables X-rays to be taken without the need for a separate connection between the detector and the X-ray generator or system. Detectors with an AED function can easily upgrade existing analog equipment to digital because they do not require a separate connection[46]. In particular, portable detectors may not be able to connect to a generator system for triggering due to the moving use environment. In addition, the faster the response time of the AED or Trigger, the better, as a longer response time after X-ray irradiation can result in a loss of dose received by the TFT Panel. Therefore, the recent trend is to embed the AED in the detector so that the detector can function similarly to the existing wired trigger without a separate connection. The sensors used for AED are primarily SiPM sensors. These sensors are known for their fast response time and magnetic field insensitivity.

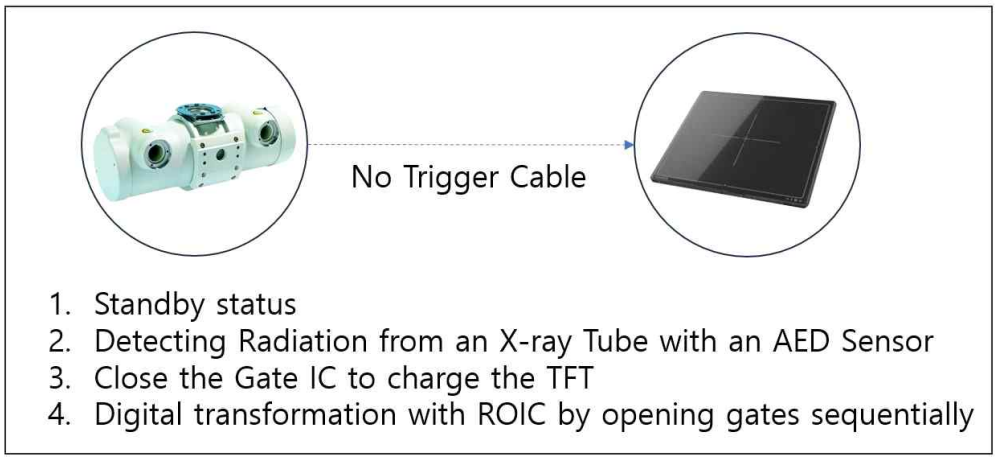

Figure 11. Operation Mechanism of AEC

2.7 Automatic exposure control (AEC)

AEC was introduced by Russell H. Morgan in 1942, applying Heinrich Rranke's (1923) theory that 'the contrast of a critical region of an image is proportional to the average contrast of the image as a whole' [47]. AEC is designed to improve image consistency across the radiation field by allowing images to be recorded using near-optimal exposures using different thicknesses, various parts of the body, and different tube potentials. It is a radiation dose control system that automatically terminates the exposure when the set incident dose is reached according to the set Air-Kerma level at the imaging receptor[48][49]. AEC can be divided into the indirect phototimer method and the direct ionizer method.

The phototimer method is an exit-type device, where the detector is positioned behind the image receptor so that radiation passes through the image receptor, as shown in Figure 12. An X-ray phosphor interacts with the radiation to generate visible light. When these photoelectrons accumulate in the condenser, they stop producing X-rays.

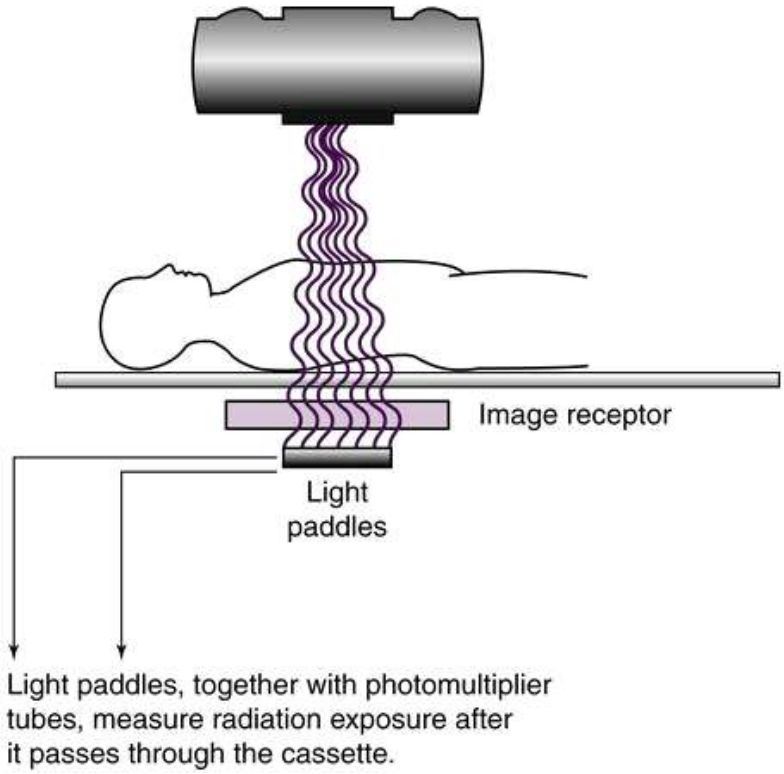

Figure 12. Phototimer Method AEC

Source: https://radiologykey.com/exposure-technique-selection/

The ionization chamber method is considered an entrance-type device in which the detector is located in front of the imaging receptor as shown in Figure 13, the detector is located in front of the image receptor and is considered as an entrance-type device, and the ionization current is controlled by detecting the X-ray-induced ionization current. The ionization chamber type is less accurate than the phototimer type, but it is less prone to failure. For this reason, most AEC systems use the ionization chamber method. [50][51]

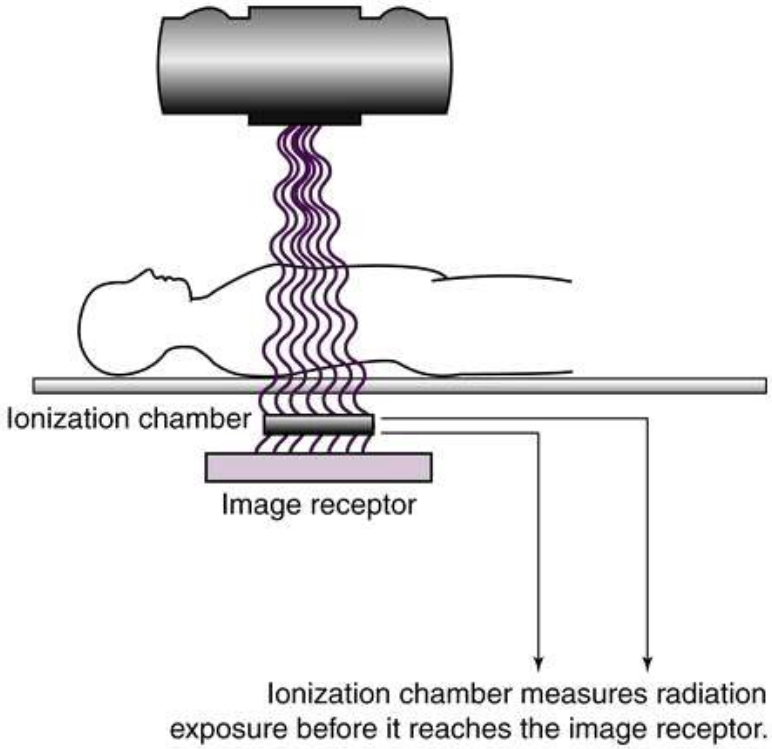

Figure 13. Ionization Chamber Method AEC

Source: https://radiologykey.com/exposure-technique-selection/

Chapter 3

Material and Methods

3.1 Experimental Environment

The common experimental environment used in this paper is shown in Figure 14. The X-ray system used in the test is the SU-3000 model, which uses Toshiba's E7252X Tube. Dosimeters, oscilloscopes, and phantoms were applied to each experimental item.

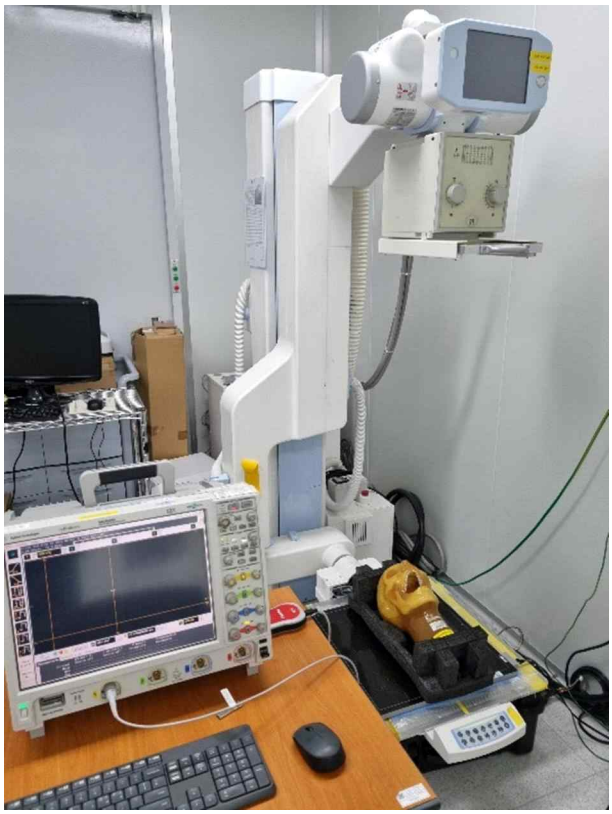

Figure 14. Experimental Environment

The dosimeter is a Piranha 657 glass dosimeter from RTI Electronics, shown in Figure 15. Piranha 657 is composed of an internal sensor with an error range of ±5% and an external sensor with a small size to minimize the influence of the image taken. The experiment was conducted using the internal sensor.

Figure 15. Piranha 657 Dosimeter

Source: Piranha_brochure

3.1.1 X-ray Exposure Test

The voltage applied to the X-ray tube determines the energy generated and affects the X-ray dose and the reduction of the patient's dose. The tube voltage measurement is designed to verify that the generator is producing exactly the kVp set on the control panel. As shown in Figure 16 the dosimeter was placed in the center of the irradiation area through the collimator with a Source to Image Receptor Distance (SID) of 150 cm.

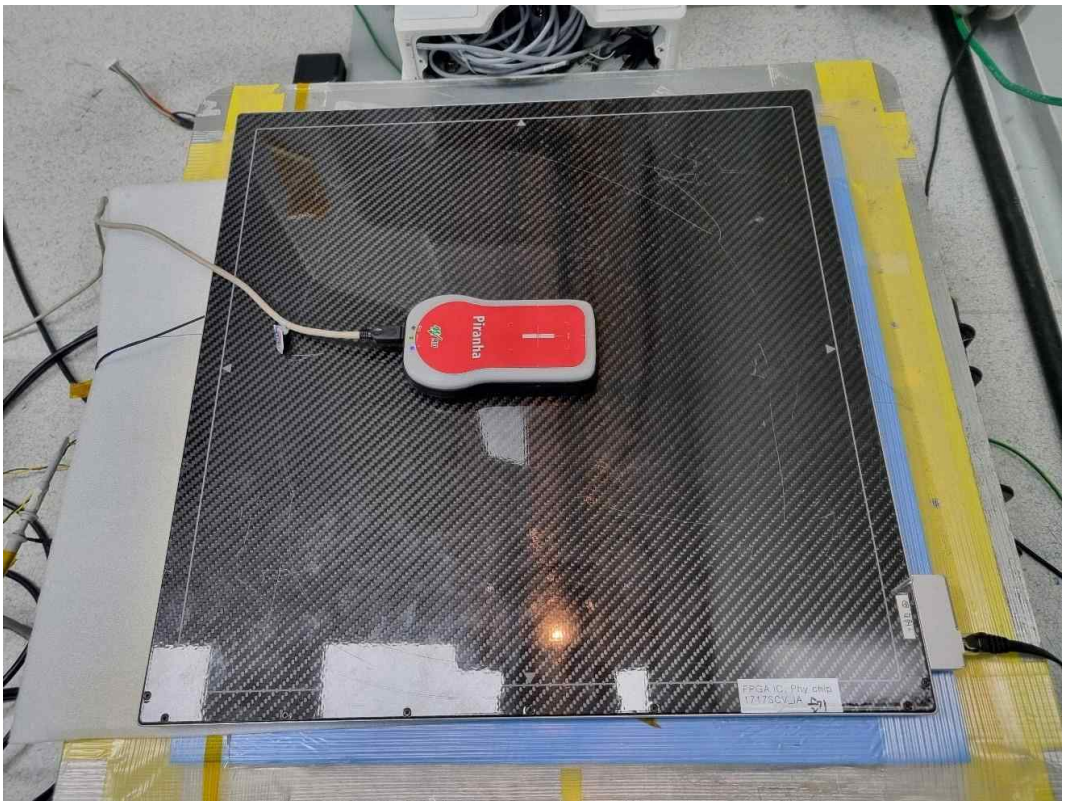

Figure 16. Exposure Test Using a Dosimeter

3.1.2 Dosimeter Testing for Tube Current, Tube Voltage

To measure the X-ray dose according to the change of tube current, the conditions of tube voltage 75 kVp and exposure time 10 mS were fixed, and the tube current was varied from 32 to 220 mA and measured with a dosimeter. The tube voltage, exposure time, and exposure (?Gy) were measured and the difference from the set tube voltage was checked.

As shown in Table. 2, we can see that the exposure value increases as the tube current increases. However, as a result of measuring the tube voltage, it was found that a difference of up to 3.2 kV remained from 1.7 to 3.2 kV compared to the set 75 kVp. Although the error is about 3%, the X-ray system used in the test can be adjusted in 1kV increments, so we conducted a confirmation test according to the change in the supply voltage.

Table. 2 Measuring Exposure as Tube Current Changes

mA Setting	Measurements			kVp Difference (kV)
	Tube voltage (kV)	Exposure time (ms)	Exposure (μGy)	
32	73.3	10.0	4.7	**1.7**
50	72.1	10.0	7.2	**2.9**
71	72.7	10.1	10.4	**2.3**
90	72.2	9.5	13.3	**2.8**
110	71.8	9.5	16.1	**3.2**
140	72.6	9.5	20.7	**2.4**
160	72.4	9.5	23.1	**2.6**
180	72.5	9.5	26.4	**2.5**
200	72.5	9.5	28.9	**2.5**
220	72.2	9.5	32.0	**3.0**

To measure the X-ray dose according to the tube voltage change, the condition of 1mAs (100mA, 10mS) was fixed and the tube voltage was varied from 50~150kV and measured with a dosimeter. Table. 3 shows the measured values of tube voltage, exposure time, and exposure (μGy), and the difference from the set tube voltage was checked. To further confirm the difference in tube voltage, a graph chart was acquired and shown in Figure 17.

Table. 3 Measuring Exposure as Tube Voltage Changes

mA Setting	Measurements			kVp Difference (kV)
	Tube voltage (kV)	Exposure time (ms)	Exposure (μGy)	
50	48.4	9.5	5.1	1.6
60	57.8	9.5	8.5	2.2
70	67.5	10.1	12.4	2.5
80	76.9	9.5	16.7	3.1
90	86.7	10	21.8	3.3
100	95.8	10.1	26.8	4.2
110	106.5	9.5	33.3	3.5
120	117.2	10.0	39.7	2.8
130	127.0	10.0	47.6	3.0
140	137.0	10.0	55.9	3.0
150	147.4	10.0	64.2	2.6

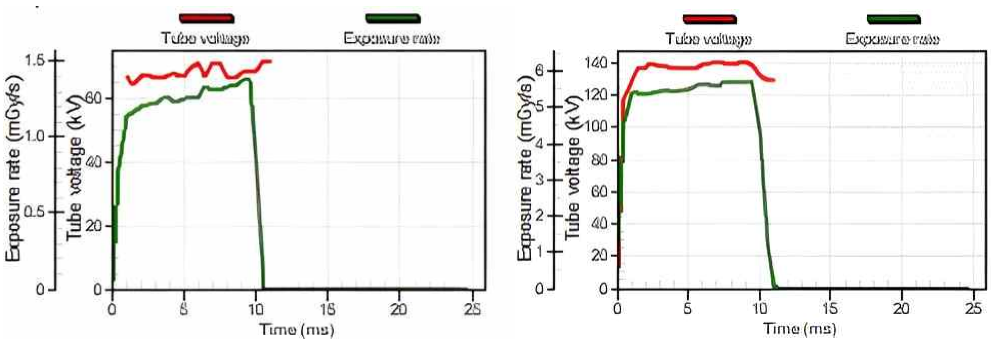

(a) (b)

Figure 17. Dosimetry charts as a function of tube voltage

(a) 70 kVp (b) 140 kVp

The tube voltage change measurements also showed a difference of 1.6 up to 4.2 kV. Upon reviewing the dosimeter graph chart, it was discovered that the tube voltage was initially set 10 - 20 % lower than the intended voltage and gradually increased during the irradiation process. Therefore, it is believed that an exposure time of 10ms or more is required for accurate tube voltage measurement of the X-ray tube. To confirm this, we conducted an additional test of changing the tube voltage at 10ms (100mA, 100mS).

Table. 4 Exposure measurement for tube voltage change after 10 mAs fixation

mA Setting	Measurements			kVp Difference (kV)
	Tube voltage (kV)	Exposure time (ms)	Exposure (μGy)	
50	49.4	99.4	32.0	0.6
60	60.2	99.4	51.9	-0.2
70	70.1	99.4	73.2	-0.1
80	79.7	99.4	98.2	0.3
90	89.5	99.9	125.2	0.5
100	98.4	99.9	155.6	1.6
110	108.3	99.8	189.4	1.7
120	118.4	99.9	225.3	1.6
130	130.0	99.9	266.2	0.0
140	140.1	94.4	289.1	-0.1
150	150.0	99.9	351.7	0.0

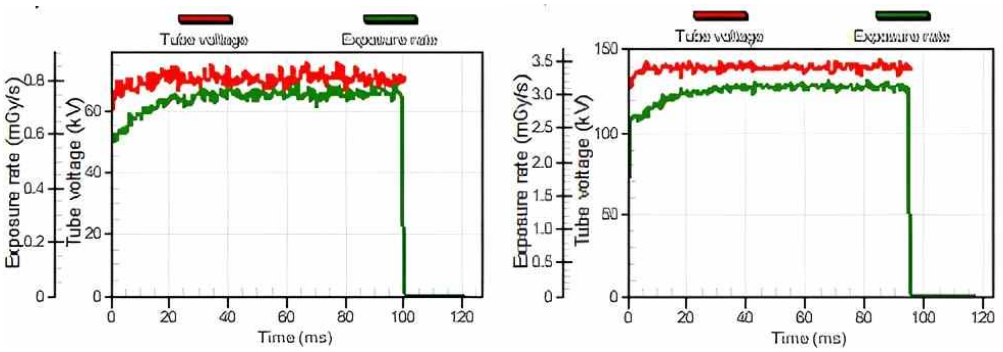

Figure 18. 10 mAs fixed, dosimetry plots as Tube voltage varies
(a) 70 kVp (b) 140 kVp

When we fixed the exposure time to 100 mS and gave a tube voltage of 0.2 to 1.7 kVp, we saw a good variation. We found that the exposure (μGy) increased linearly with the increase of tube voltage and tube current. Checking the dosimeter graph chart in Figure 18, we checked the dosimeter graph chart, we found that the tube voltage changed by about 20ms after the start of the irradiation, which means that it is important to secure the minimum exposure time for stable exposure measurements. Figure 19. (a) measures the dose as the line voltage changes, and Figure 19. (b) shows the change in dose as the line current changes, showing a linear increase.

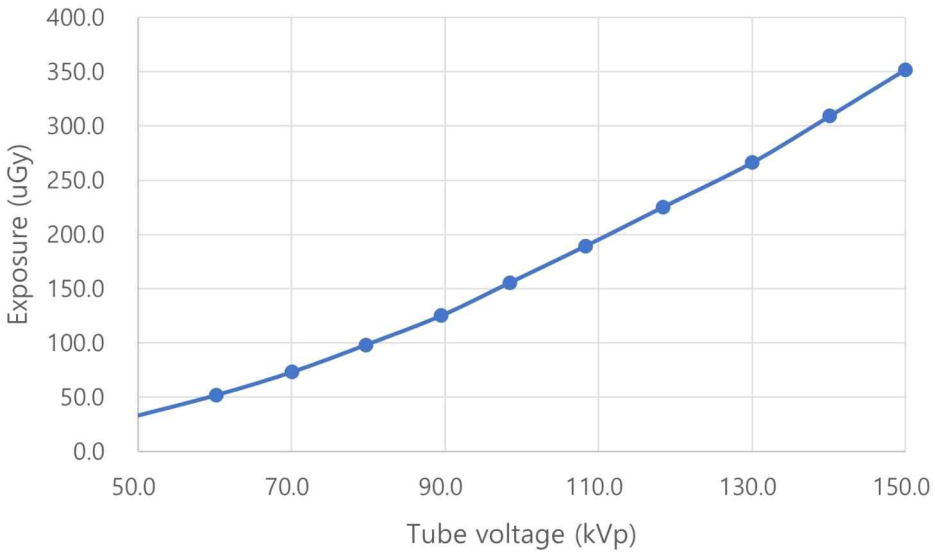

(a)

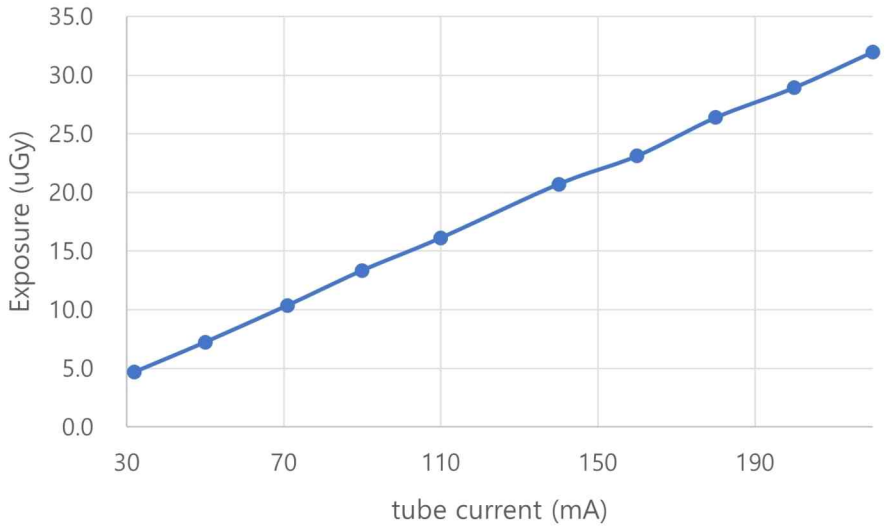

(b)

Figure 19. Exposure change chart as a function of Tube voltage and tube current (a) tube voltage (b) tube current

3.1.3 Test the Linearity of the Generator System

Before the full-scale experiment, the accuracy and reproducibility of the X-ray Generator System was checked with a dosimeter. To check the accuracy of the tube voltage, 20 measurements were made with 70 kVp, and the results shown in Figure 20. and the average of the measurements was 69.8 kVp, confirming that the calculation result was 0.3% through Percent Average Error (PAE).

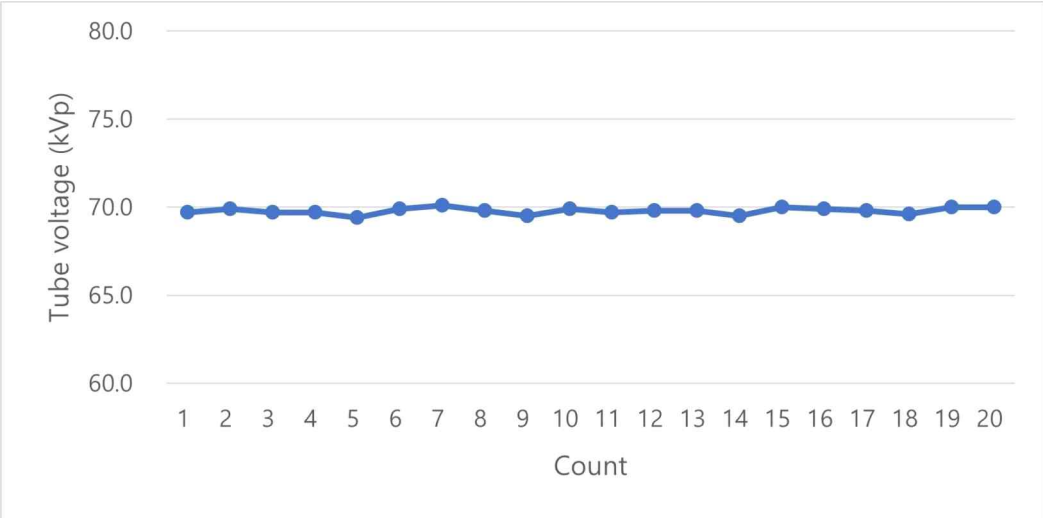

Figure 20. Tube voltage measurement reproducibility

3.2 Evaluate SiPM Characterization

3.2.1 Evaluate SiPM Sensor Characteristics

A simple representation of the internal structure, including the SiPM, is shown in Figure 21. The dose of the irradiated X-ray is attenuated as it passes through the scintillator, panel, and middle block, which means that the material or shape of the middle block also causes differences in the dose received by the SiPM Sensor. Therefore, the test of Case 2 in Figure 21. (b) was also tested in parallel.

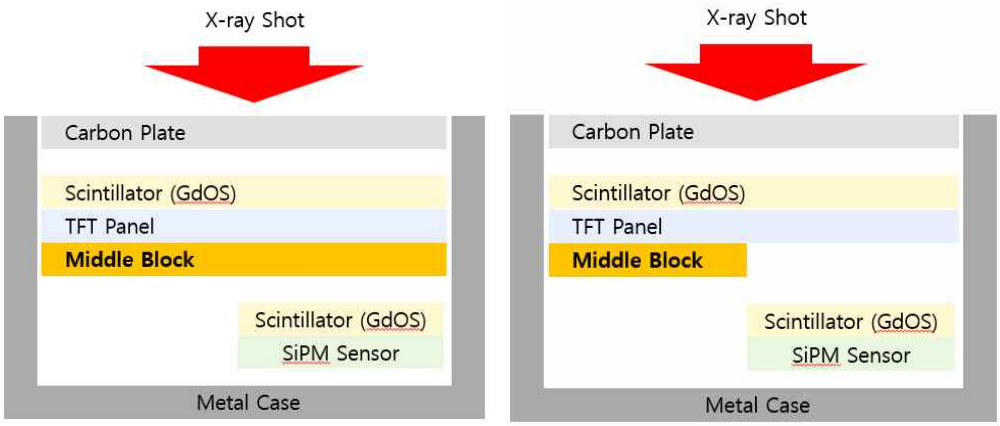

(a) (b)

Figure 21. SiPM Dose Detection test

(a) Case 1: With middle block. (b) Case 2 : Without Middle block.

Figure 22. (a) A bucky with a motor was used to perform magnetic field testing because handheld detectors are highly vulnerable to magnetic fields generated by external shocks or peripheral devices. Seven sensors from five manufacturers were selected and tested. Figure 22. (b) A sensor EV board provided by the manufacturer was used to compare response time and dose detection characteristics.

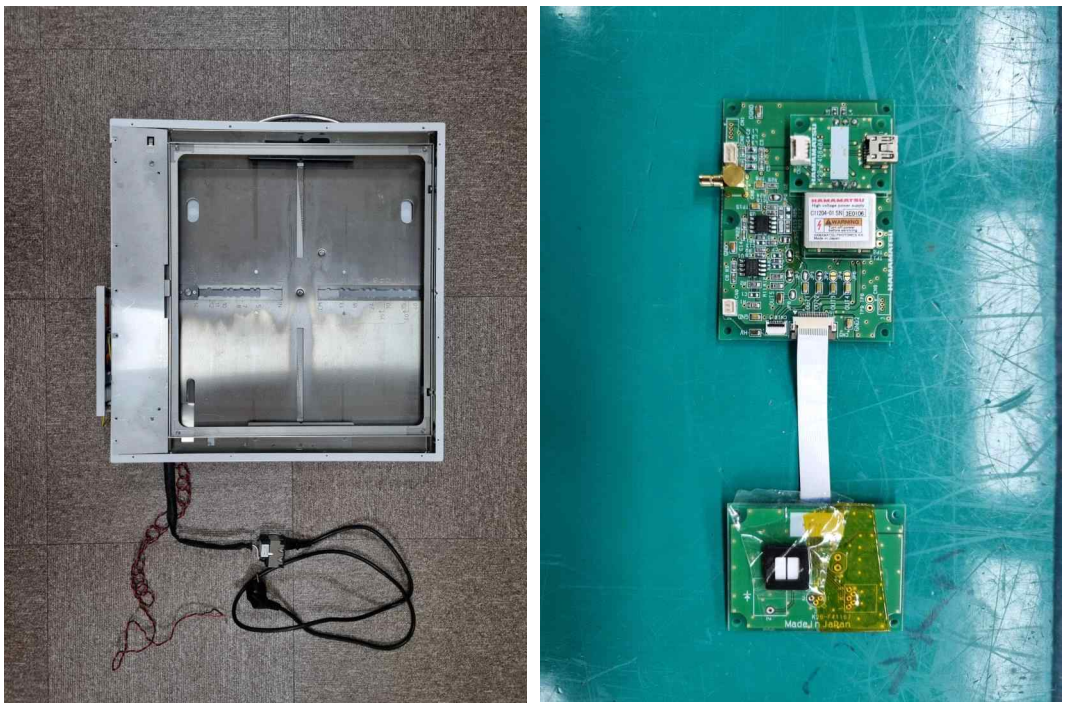

(a) (b)

Figure 22. SiPM Characterization Test Materials

(a) Bucky for Magnetic Field Test (B) SiPM Sensor EV Board

Table. 5 shows the characteristics of each sensor, and all sensors showed high robustness to the surrounding environment by not responding to magnetic fields and external shocks due to the characteristics of SiPM itself. In the sensitivity measurement part, in Figure. 21 (a), all sensors did not respond due to attenuation by the middle block. In the condition of Figure 21. (b), where the middle block on the top of the SiPM was removed, 3 to 7 sensors responded, and the response times were all measured below 10 ns. The response time is the reaction time of the sensor after X-ray irradiation, and the longer the time is, the faster the better, as the dose received by the TFT panel is lost. The photosensitizer directly affects performance because it converts X-rays into visible light, so it was necessary to

compare Sensors 1 through 5, which detect visible light, with Sensors 6 through 7, which are made exclusively for X-ray detection and have a built-in photosensitizer.

Table. 5. Analysis of SiPM Characteristics

	1	2	3	4	5	6	7
Manufacturer	A	B	C		D	E	
Sensing Source	Light	Light	Light	Light	Light	X-ray	X-ray
Operating Voltage	3.3VDC	3.3VDC	27VDC	27VDC	53VDC	60VDC	60VDC
Response Time	>100 ms	>100 ms	<10 ns	<10 ns	<10 ns	<10 ns	<10 ns
Op Amp	O	O	X	X	O	X	X
Sensitivity Case1	X	X	X	X	X	X	X
Sensitivity Case2 (Peak Voltage)	X	X	O (40mV)	O (400mV)	O (150mV)	O (30mV)	O (30mV)
Mechanical Shock Resistor	O	O	O	O	O	O	O
Magnetic Field Resistor	O	O	O	O	O	O	O

As for the X-ray dose condition, in order to check the detection of high-sensitivity dose, the system's minimum irradiation condition and Source to Detector Distance (SDD) were set to 150 cm, and an Al 21 mm filter was added to check the detection and output peak voltage for the ultra-low dose environment of 10 nGy dose. With the ultra-low dose of 10 nGy, the Gadolinium Oxide (GaOS) sensors used in the experiment and the sensors in Sensors 6 and 7 are judged to have similar performance. Figure 23. is a waveform confirming the low-dose section for Sensor No. 4 in Table. 4. Approximately 410 mV at 10 nGy and 590 mV at 20 nGy were measured, confirming that it is possible to distinguish through the voltage level.

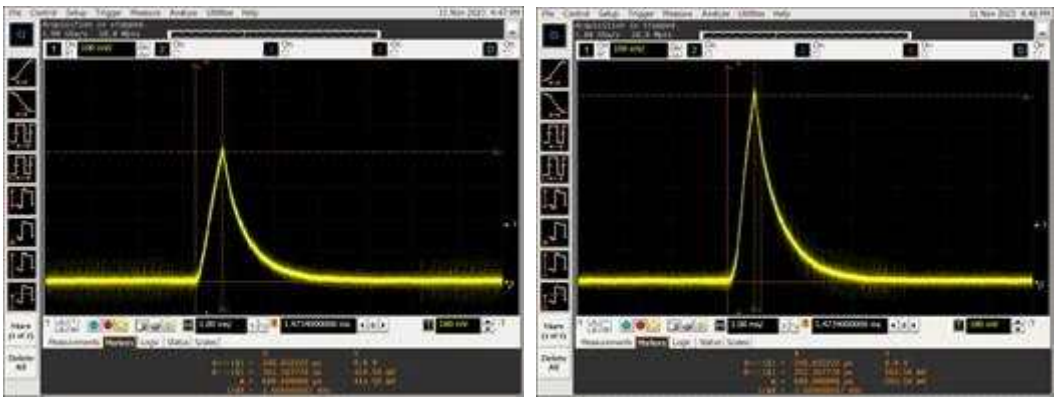

(a) (b)

Figure 23. Extremely Low Dose Tests (a) 10 nGy (b) 20 nGy

Based on the results of these tests, it was determined that Sensor 4 of Company C, with an output level for a dose of 10 nGy and a fast response time of 10 ns or less, was the most suitable for the intended use.

3.2.2 Characteristic test by Tube voltage, Tube current

As a test to check the change of SiPM Signal Voltage according to the X-ray tube voltage, the X-ray tube current was fixed at 5mAs (50mA, 100ms) and the output was checked according to the change of X-ray tube voltage. The X-ray tube voltage was investigated by setting 50 kVp ~ 180 kVp. Figure 24. (a) and (b) show the output of the SiPM.

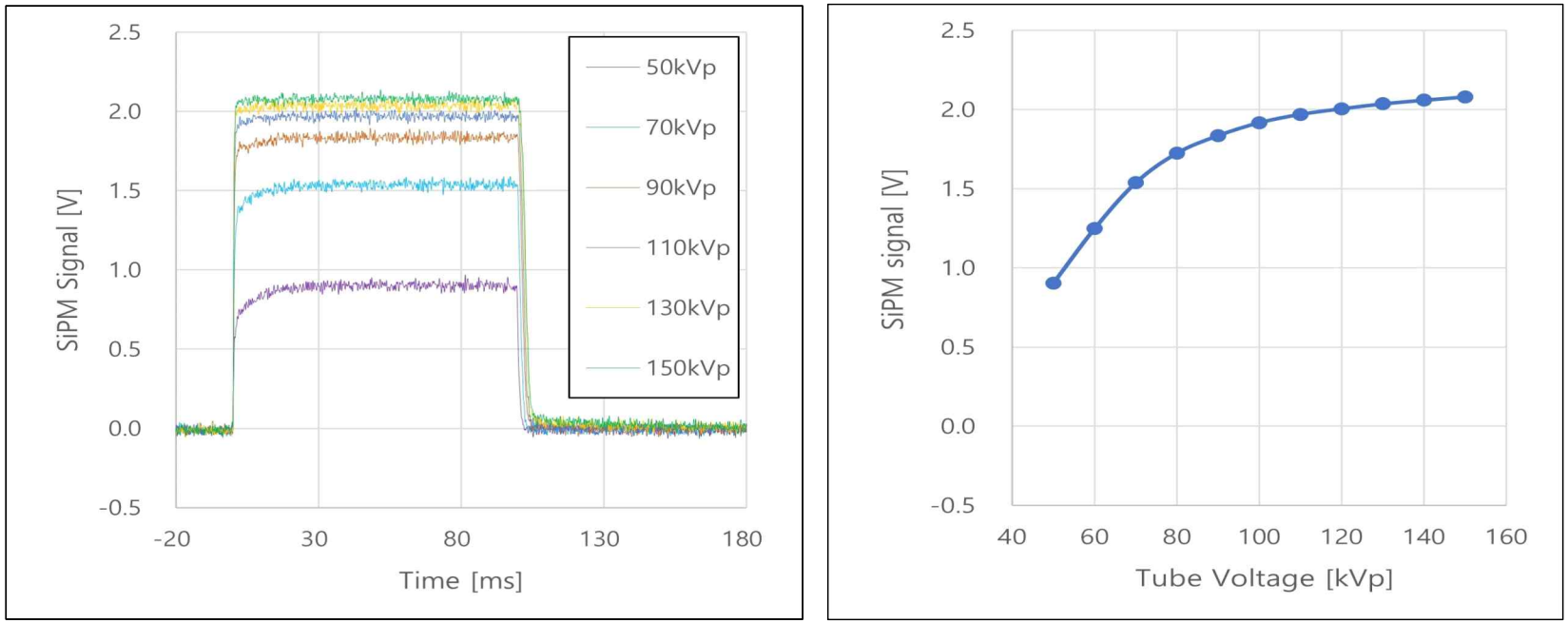

(a) (b)

Figure 24. SiPM Signal Voltage Variation with Tube Voltage (a) SiPM Output Comparison (b) Variation Chart

As a test to check the change of SiPM Signal Voltage according to the X-ray tube current, the X-ray tube voltage was fixed at 70kVp and the output was checked according to the change of X-ray tube current. The X-ray tube current was set from 4.0 mAs to 16.0 mAs. The irradiation time was fixed at 100ms to check the change in current. Figure 25. (a) and (b) show the output of the SiPM.

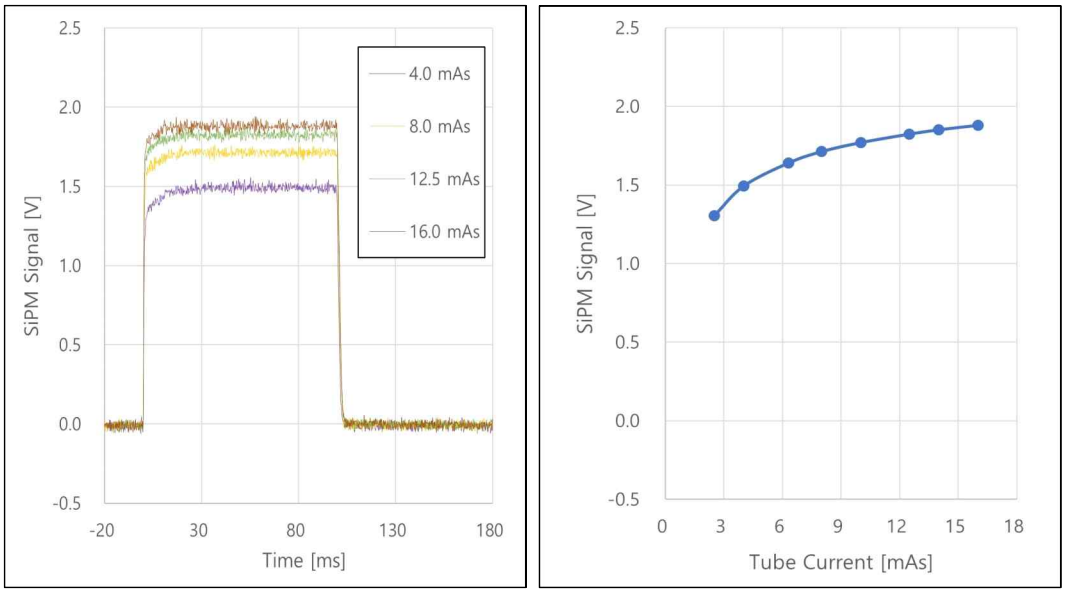

Figure 25. SiPM Signal Voltage Variation with tube Current
(a) SiPM Output Comparison (b) Variation Chart

To confirm the correlation of SiPM's output with X-ray dose, a confirmation test was conducted by changing each factor of tube voltage and tube current. The measured results are shown in Table. 6, and the chart is shown in Figure 26. The test results confirmed the theoretical background that the higher the tube voltage and tube current, the higher the average energy of the X-ray photon, and the dose increases proportionally to the square of the tube voltage V, the tube current, and the irradiation time t, and the signal of the SiPM has a similar signal. However, it is judged that there are additional factors to consider, such as the

dose attenuation caused by passing through the scintillator and panel, and the reaction characteristics of the scintillator and SiPM.

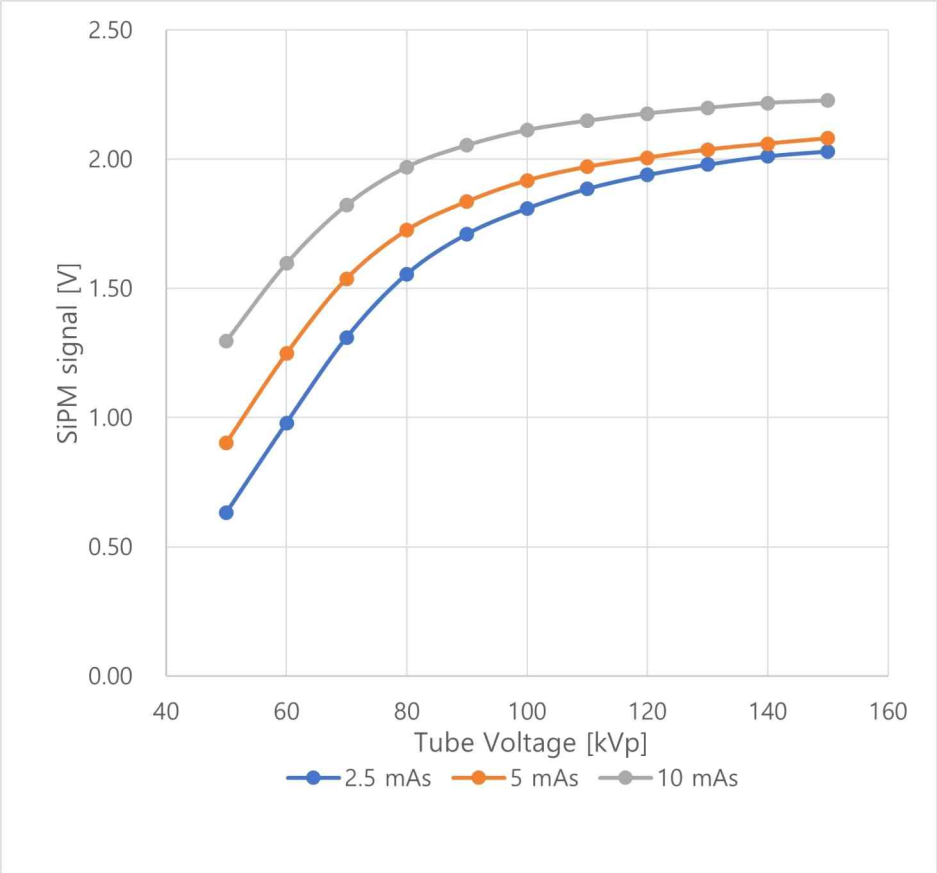

Figure 26. Output chart of SiPM as a function of X-ray dose

Table. 6 Signal level(Voltage) of SiPM based X-ray dose conditions

	50 kVp	60 kVp	70 kVp	80 kVp	90 kVp	100 kVp	110 kVp	120 kVp	130 kVp	140 kVp	150 kVp
2.5 mAs	0.6 V	1.0 V	1.3 V	1.6 V	1.7 V	1.8 V	1.9 V	1.9 V	2.0 V	2.0 V	2.0 V
5.0 mAs	0.9 V	1.3 V	1.5 V	1.7 V	1.8 V	1.9 V	2.0 V	2.0 V	2.0 V	2.1 V	2.1 V
10.0 mAs	1.3 V	1.6 V	1.8 V	2.0 V	2.1 V	2.1 V	2.2 V	2.2 V	2.2 V	2.2 V	2.2 V

Chapter 4

Results and Analysis

4.1 Evaluate imaging quality

The image evaluation followed the test methods outlined in IEC 62220-1(Table 7) and was tested according to RQA 5 of RADIATION QUALITY (IEC 61267:1994) to determine DETECTIVE QUANTUM EFFICACY and corresponding parameters.

Table 7. IEC 62220-1 RQA chart

Radiation Quality No.	Approximate X-ray Tube Voltage [kV]	Harf-Value Layer (HVL) [mm Al]	Additional Filtration [mm Al]
RQA3	50	4.0	10.0
RQA5	70	7.1	21.0
RQA7	90	9.1	30.0
RQA9	120	11.5	40.0

For each X-ray system, it is the HALF-VALUE LAYER value of the 7.1 mm AI that is important for RQA, not the kV condition, due to usage conditions, tube aging, etc. Based on this, images were acquired and measured with a dosimeter in the same environment as shown in Figure 16. Table 8 shows the data measured by the dosimeter during image acquisition.

Table. 8 Dosimetry measurements for image acquisition by dose

Tube voltage (kV)	Exposure time (ms)	Exposure (μGy)	HVL (mm Al)	Total filtr. (mm Al)
73.0	3.0	0.1	7.5	32.0
75.5	7.0	0.2	6.8	20.3
72.9	12.6	0.4	7.1	25.2
75.1	19.5	0.6	6.7	19.4
71.7	26.1	0.8	7.2	28.2
72.5	33.1	1.1	7.1	26.1
73.7	49.2	1.6	7.3	27.1
75.8	49.2	2.0	7.1	22.5
74.0	49.2	2.1	7.2	25.7
74.5	49.2	2.6	7.0	22.8
73.9	49.2	3.2	7.2	25.5
73.4	49.2	3.2	7.2	26.0
72.7	49.7	4.1	7.2	27.3
74.5	49.2	4.1	7.2	24.8
72.5	49.2	5.2	7.3	28.5
74.2	49.2	6.5	7.1	24.1
74.4	49.2	9.2	7.2	24.6
73.7	49.2	11.9	7.1	24.7
74.2	70.2	19.0	7.1	24.6
74.3	98.9	27.2	7.2	24.6
74.3	139.0	38.5	7.1	24.4
74.5	159.6	44.3	7.1	24.2

4.1.1 SNR Analysis

The SNR measurement is calculated by taking dose-specific air images and calculating the ADU value of the acquired image. The image type of the detector used in the test is 14 bit, and the ADU representation range is 0 to 13201. A dosimeter is placed in the center of the detector to measure the irradiated X-ray dose in μGy, and the ADU value is calculated by checking the ADU value for the area near the dosimeter. Figure. 28 (a) The air image taken by placing the dosimeter shows the ADU value for the measurement area, and (b) is the output graph chart of the dosimeter. With the RQA5 X-ray beam quality fixed and mAs varied, the dose measured by the dosimeter and the image ADU are substituted into Equation (4) to calculate the SNR[52]. Figure 27 (a) shows the $Signal\,Power$ and $Noise\,Power$ of the formula, while the average (ave) and deviation (dev) values are displayed in Fig.

$$SNR = 20\log\left(\frac{Signal\,Power}{Noise\,Power}\right) \tag{4}$$

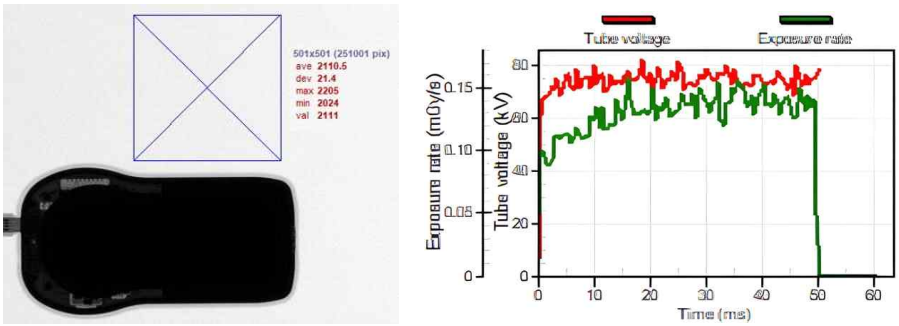

(a) (b)

Figure 27. SNR analysis (a) ADU value of the acquired image and measurement area (b) Dosimeter chart

The SNR measured as a function of dose is shown in Figure 28. The higher the SNR, the less signal-to-noise, and it increases with the absorbed dose but remains the same above a certain level.

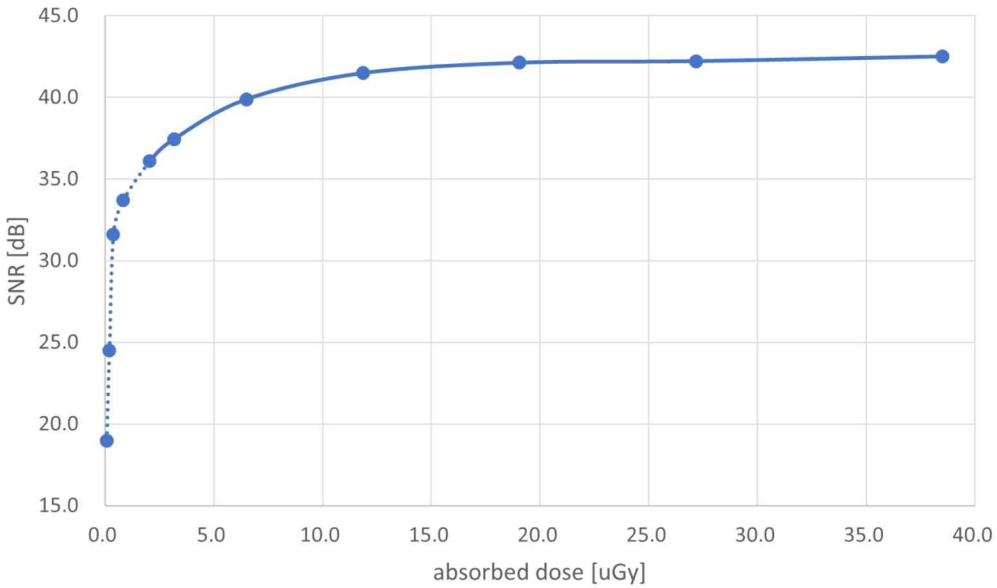

Figure 28. SNR measurement chart

4.1.2 NPS Analysis

Figure 29 shows an NPS measurement chart. The NPS can be calculated using a two dimensional fast Fourier transform of flat field images (corrected for gain offset) of a 500 x 500 area used for SNR calculation. In 2D images, noise of the same magnitude has a greater impact when the object is small and becomes difficult to distinguish visually. Therefore, noise should also be measured and evaluated through a metric that is combined with spatial resolution[53][54]. You can see the noise distribution for each frequency.

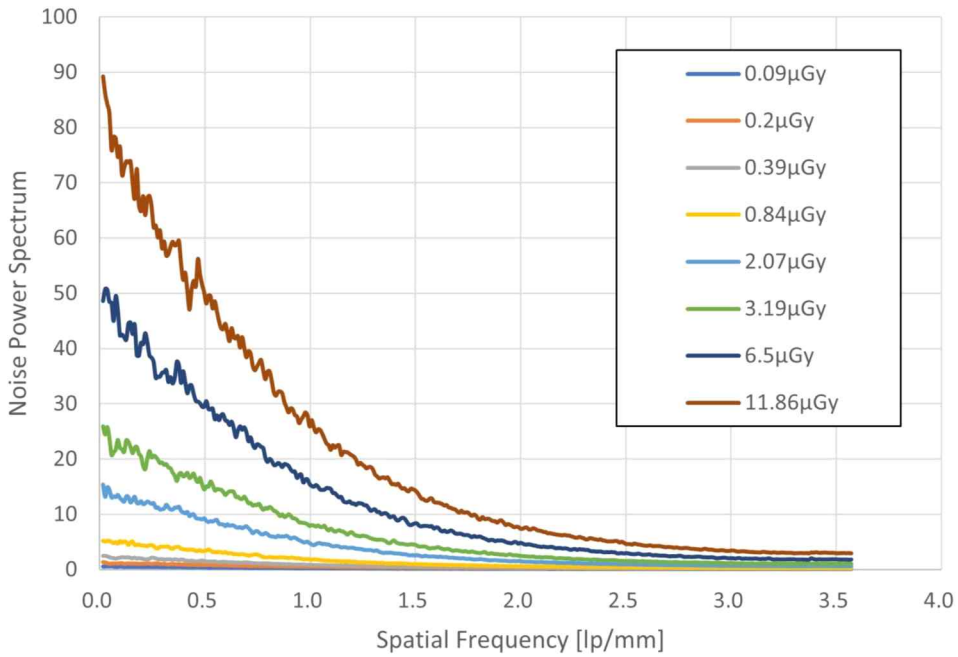

Figure 29. NPS measurement chart

4.1.3 MTF Analysis

MTF is a factor that can be used to simultaneously represent contrast and spatial resolution using edge phantoms. MTF measurements were performed using the "tilted edge" technique, which analyzes the edge portion of the image generated by placing an edge phantom in the detector imaging area and acquiring an image[55]. Figure 30, (a) is the raw image of the edge phantom, which shows the ADU value of the edge part, and (b) is the MTF measurement chart. The measurement shows a 62% MTF with an error range of ± 2%, which is within typical detector performance deviations. Typical detector resolution specifications are shown based on 1 lp/mm.

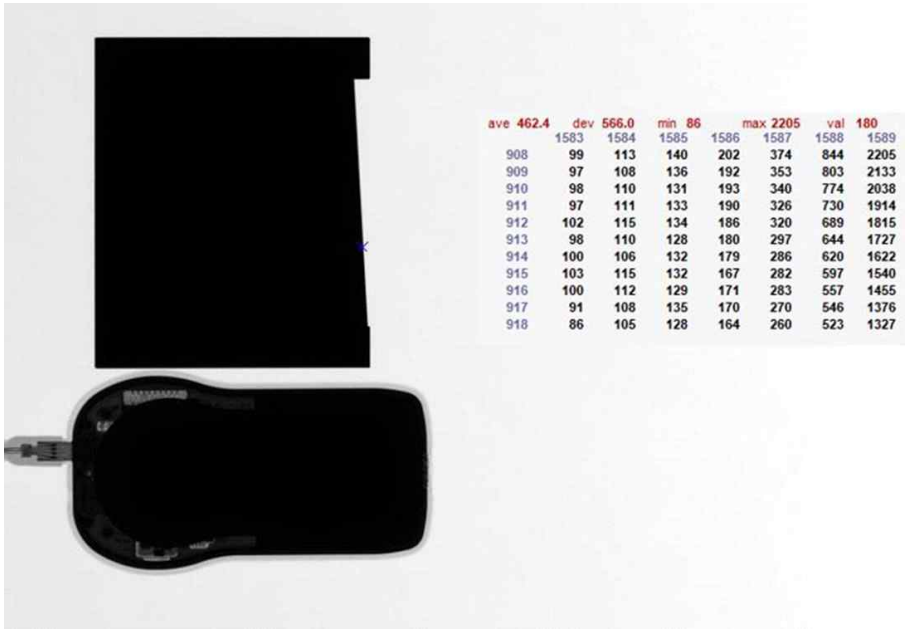

(a)

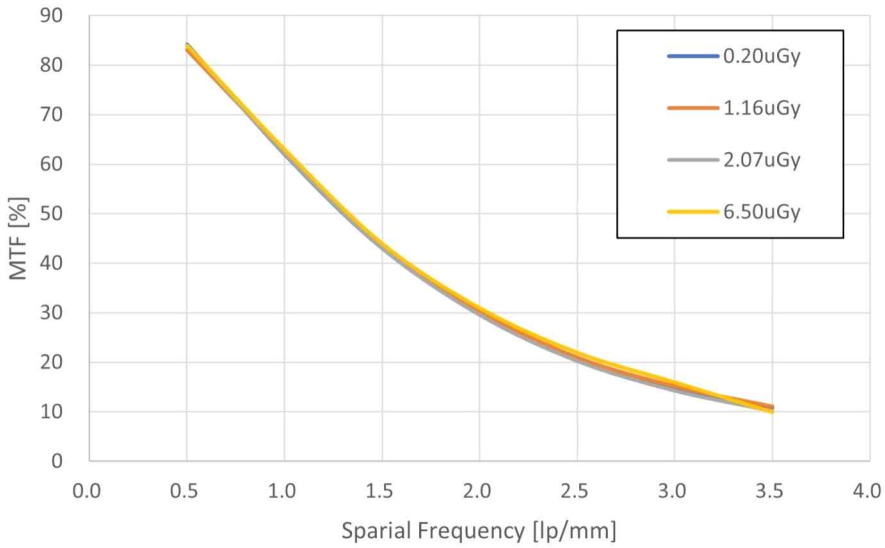

(b)

Figure 30. MTF measurement (a) raw image (b) MTF chart

4.1.4 DQE Analysis

For doses above 2.07 μGy, the detector image quality metric, DQE performance, reaches a maximum of 68% in Figure 31 shows that the DQE performance reaches a maximum of 68%. For doses higher than 2.07 μGy, from 3.19 to 11.86 μGy, the DQE is equivalent and does not improve. Therefore, in actual clinical imaging, if the dose penetrating the human body and entering the detector is around 2.07 μGy, the image quality can be considered the best image the detector can produce.

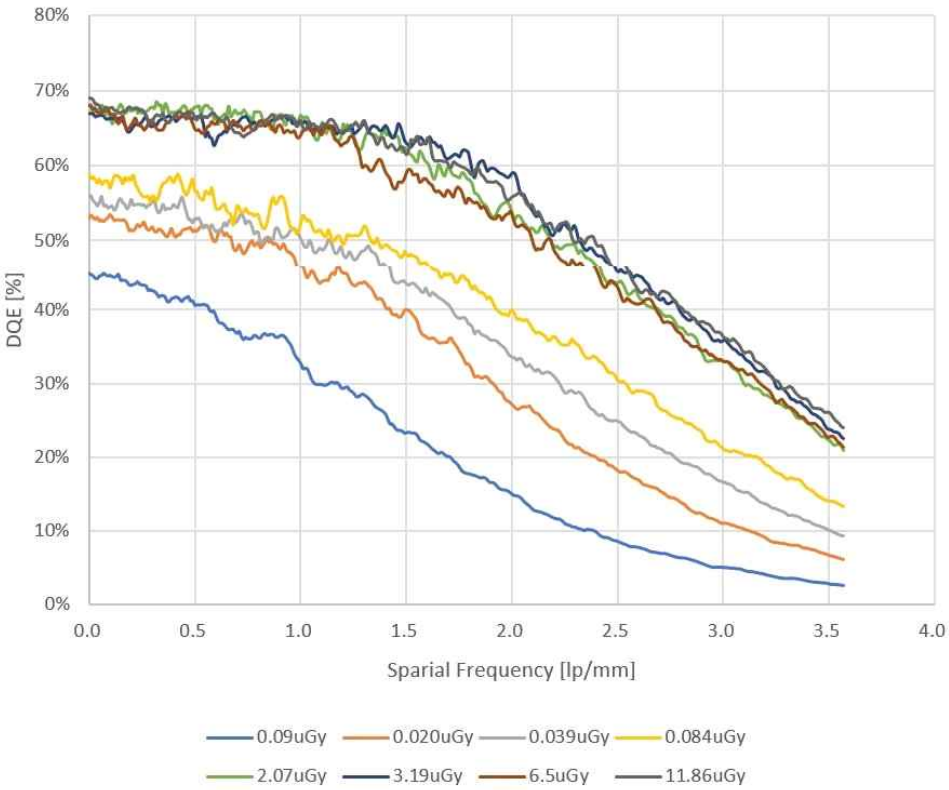

Figure 31. DQE Chart

4.2 SiPM Dose Calculation

Since the optimal dose was identified through the DQE analysis of the detector, the signal of the image ADU and SiPM at each dose was measured (Table 9.), yielding the values shown in Equation (5). Where v and s are ㎷ and ㎳ of SiPM. We verified that the error of this formula is ±4%. Figure 32 is a comparison chart of the ADU calculated from the image and the formula.

Table 9. Image ADU and SiPM Signal by Dose

Dosimeters	Image	SiPM		Calculated Value
Dose [μGy]	[ADU]	[V]	[ms]	[ADU]
0.09	27.5	0.49	3	25.4
0.20	61.8	0.65	7	63.3
0.59	230.6	0.81	19	248.8
1.13	420.1	0.81	35	435.9
1.16	550.7	0.81	49	599.6
2.07	675.1	0.84	49	667.0
2.55	844.7	0.93	49	899.8
5.15	1694.3	1.17	49	1776.8
11.86	3796.6	1.52	49	3878.0
27.18	8624.5	1.57	99	8528.8
38.50	12021.7	1.56	139	11708.0

$$SiPM\ ADU = (v^3 \times (s+1) \times 2) \times 11 + 15 \quad (5)$$

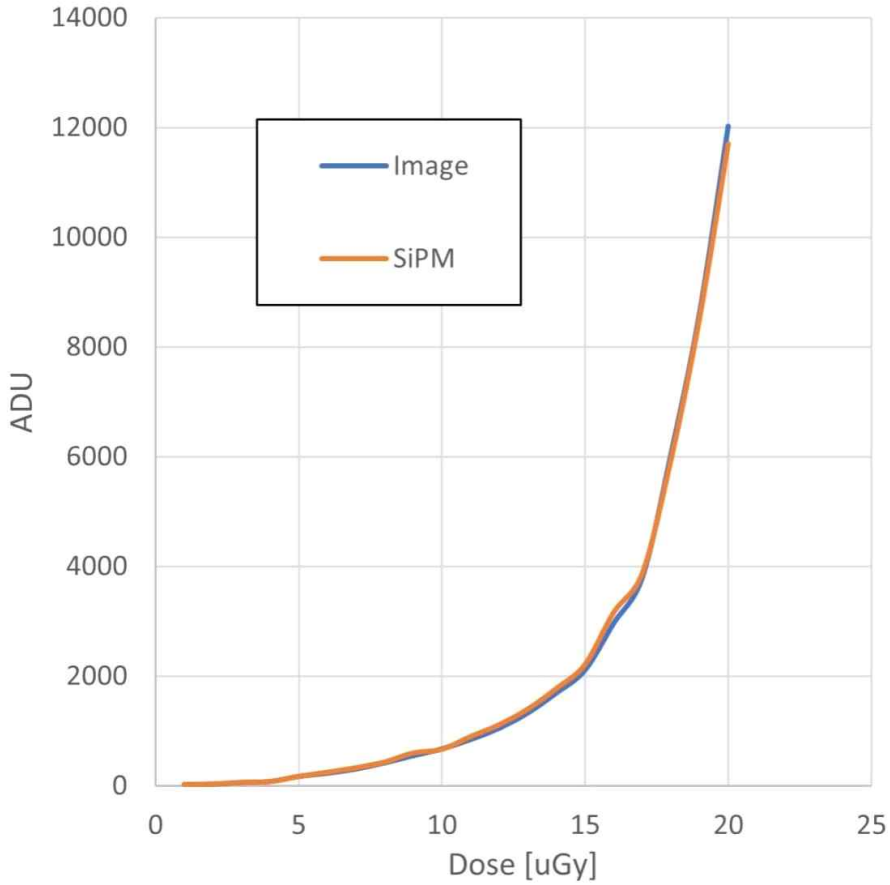

Figure 32. Comparing Image ADU readings with SiPM output

4.3 Implement optimal dose

4.3.1 Configure Hardware

The hardware for optimal dose implementation is shown in Figure 33. It consists of an MCU as a controller, a detection unit, and external connections as shown in Figure. The detection part consists of a SiPM Sensor, an amplifier, a comparator, a Set/Reset Flip-Flop for the Automatic Exposure Detection (AED) function, and an ADC part for the Automatic Exposure Control (AEC) function. It is configured to be controlled by a Photo Diode configuration for connection to an external X-ray System. The Set/Reset Flip-Flop prevents the momentary loss of the trigger signal at low doses and reduces the load on the MCU for detection.

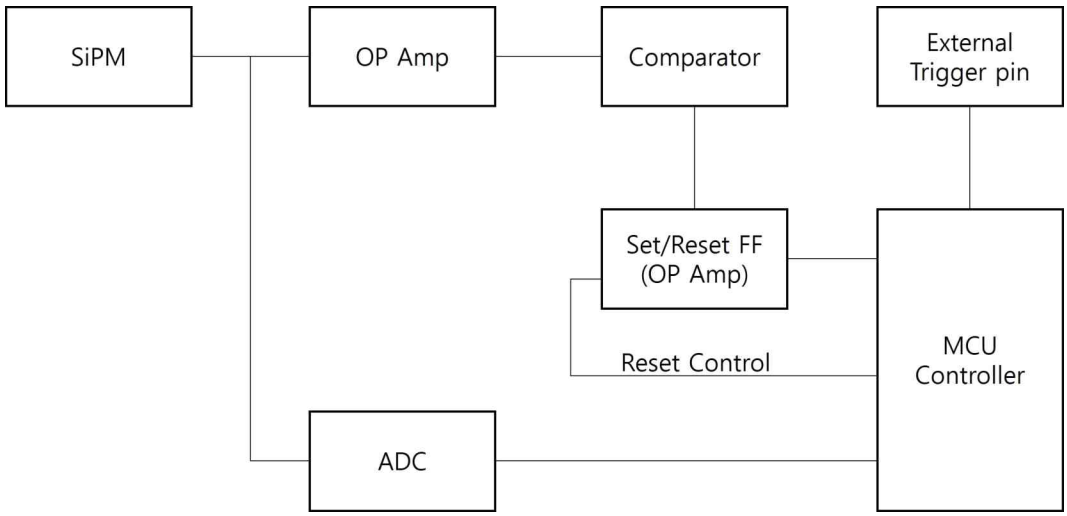

Figure 33. Hardware block diagram

4.3.2 Configure the connection

The connection between the SiPM Controller and the X-ray System for optimal dose control is shown in Figure 34. The X-ray system is equipped with the AEC mode function, but in order to exclude the variables of the system, the SiPM Controller is connected to the Hand Switch Connector in manual mode to control the X-ray irradiation without interference from the system.

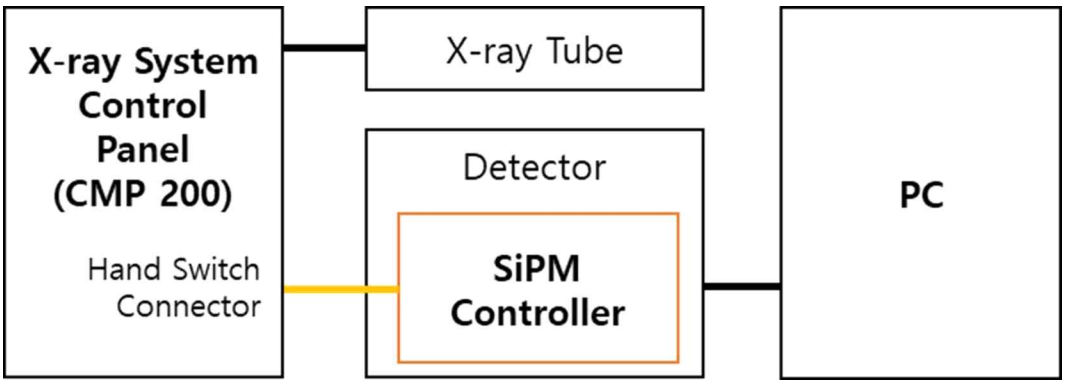

Figure 34. Connection Block Diagram

4.4 Evaluating Optimal Dose Acquisition

The X-ray System was set to manual mode and the darkest part of the nose in the Skull AP and the spine in the Chest AP were placed in the SiPM position for minimum ADU detection. The value calculated through SiPM was controlled through the Controller to stop the generator irradiation at the ADU threshold of 650.

For the Skull AP, the detector manufacturer's standard for dosimetry at 75 kVp 20 mA averages 342.8 μGy as a condition of use. Images of the standard dose and the dose controlled with the optimal dose were acquired to determine the difference. The optimal dose controlled through the SiPM was 75 kVp 8.87 mAs, which was confirmed by dosimetry to be 148.3 μGy.

Figure 35 (a) Post-processed image of the image taken with the manufacturer's standard, and (b) post-processed image taken with the optimal dose through the SiPM controller.

Figure 36, Raw images showing the ADU in the SiPM region, (a) taken with the manufacturer's standard, (b) taken with the optimal dose through the SiPM controller.

Figure 37 shows a magnified image of the orbital rim and sphenoidal bone. The radiologist's evaluation of the image was that 'imaging conditions are important for diagnosing orbital fractures or sphenoidal fractures in clinical practice, but both images show the orbital rim and sphenoidal bone well, and there seems to be no significant difference between the reference and control images that would lead to a misreading error in fracture diagnosis'. This evaluation report is attached to Figure 41 through Figure 45.

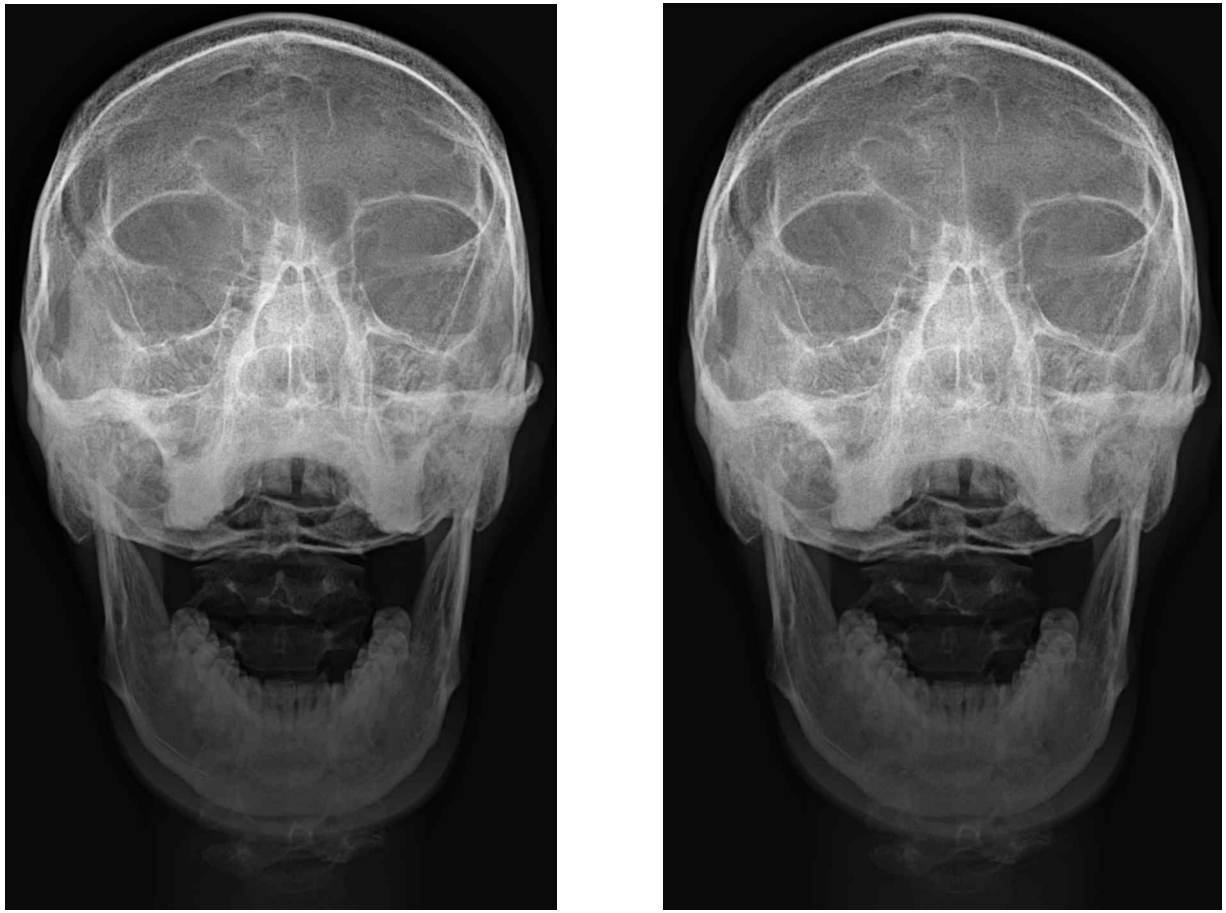

(a) (b)

Figure 35. Skull AP post-processed image (a) manufacturer's standard : 342.8 μGy (b) SiPM dose Control : 148.3 μGy

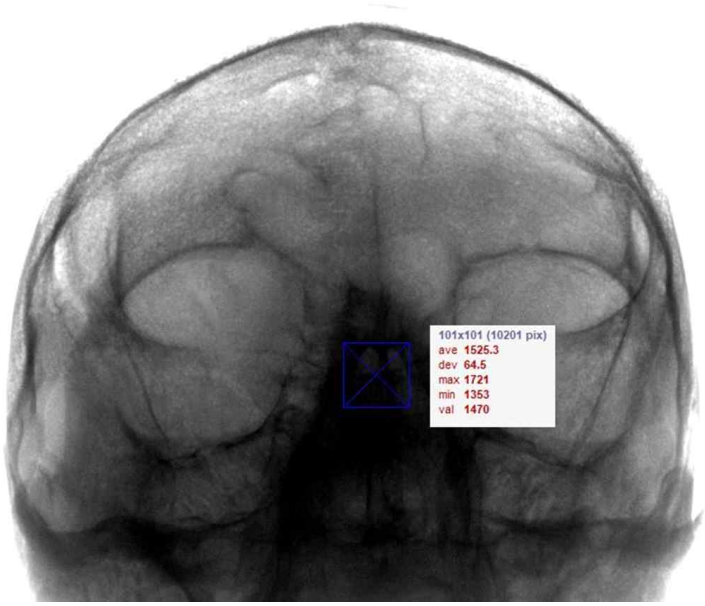

(a)

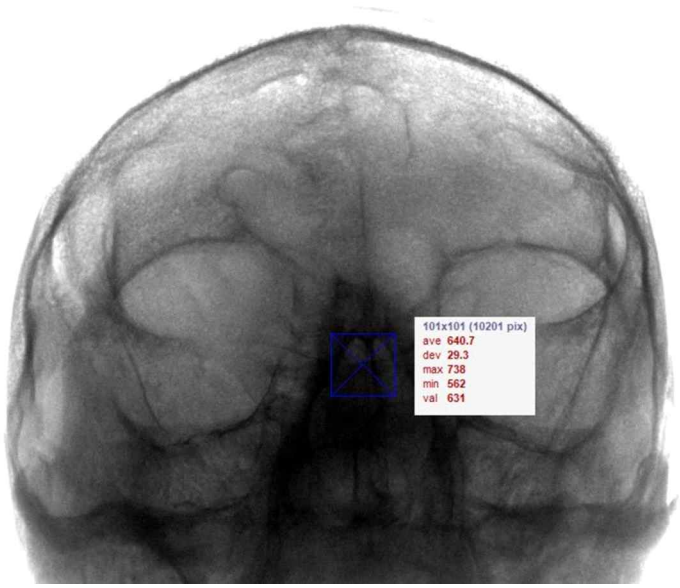

(b)

Figure 36. Skull AP raw image showing the ADU in the SiPM area (a) manufacturer's standard : 342.8 μGy (b) SiPM dose Control : 148.3 μGy

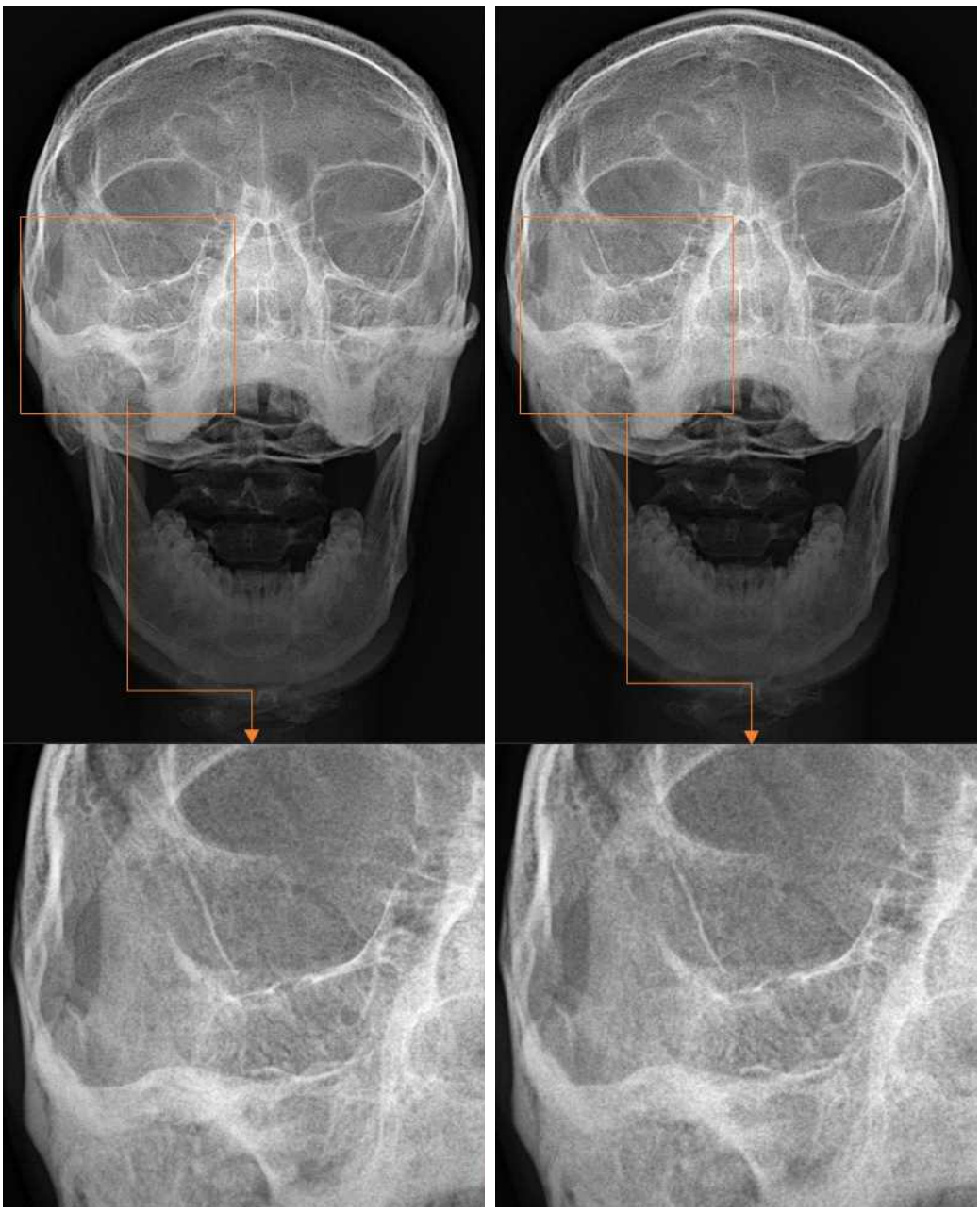

(a) (b)

Figure 37. Skull AP orbital rim and sphenoidal bone (a) manufacturer's standard : 342.8 μGy (b) SiPM dose Control : 148.3 μGy

Figure 38, Comparison images for the Chest AP, (a) post-processed image taken at the manufacturer's reference, and (b) post-processed image taken with dose control via the SiPM Controller.

Figure 39, Raw image showing the ADU in the SiPM area, (a) taken at the manufacturer's suggested criteria, (b) taken with optimal dose through the SiPM Controller. It is found that the detector manufacturer's reference is 81.9 μGy when dosimetrically measured with 120 kVp 2 mAs, and the controlled optimal dose is 27.9 μGy when dosimetrically measured with 120 kVp 0.67 mAs.

Figure 40 shows an enlarged image of the left lung. The radiologist's evaluation of the image was that 'both images have adequate bronchial representation in the hilum, and there does not appear to be a significant difference between the two images, with good visualization of the mediastinal pulmonary vessels and the spine in the projection of the mediastinum, so there is no problem with tumor shading'. This evaluation report is attached to Figure 41 through Figure 45.

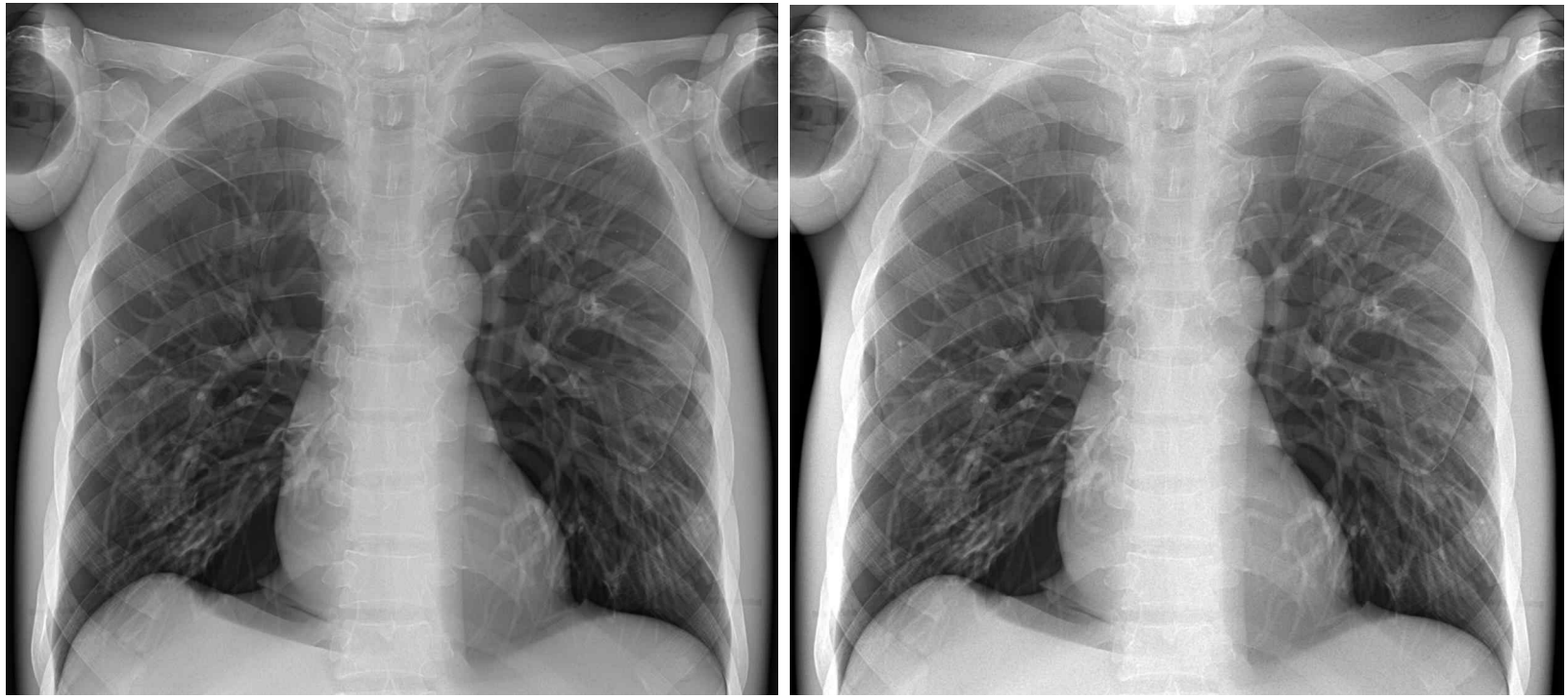

(a) (b)

Figure 38. Chest AP post-processed image (a) manufacturer's standard : 81.9 μGy (b) SiPM dose Control : 27.9 μGy

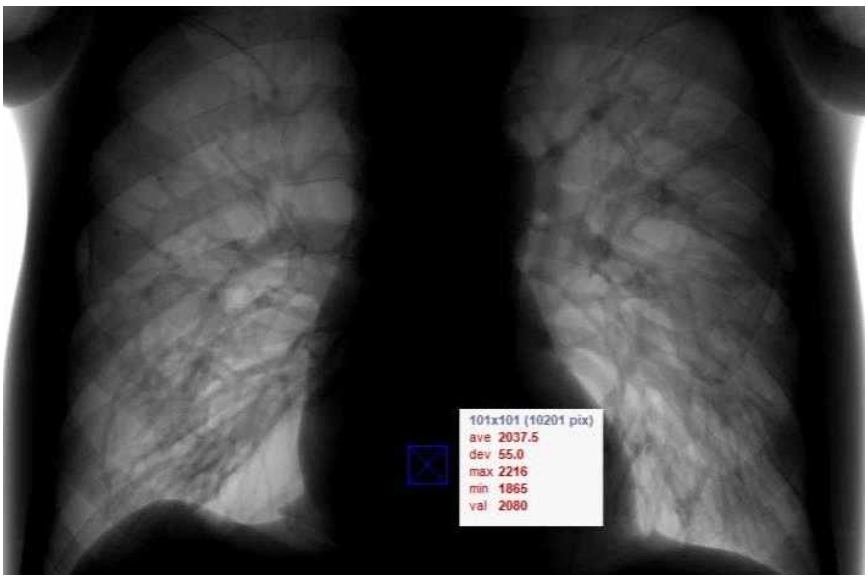

(a)

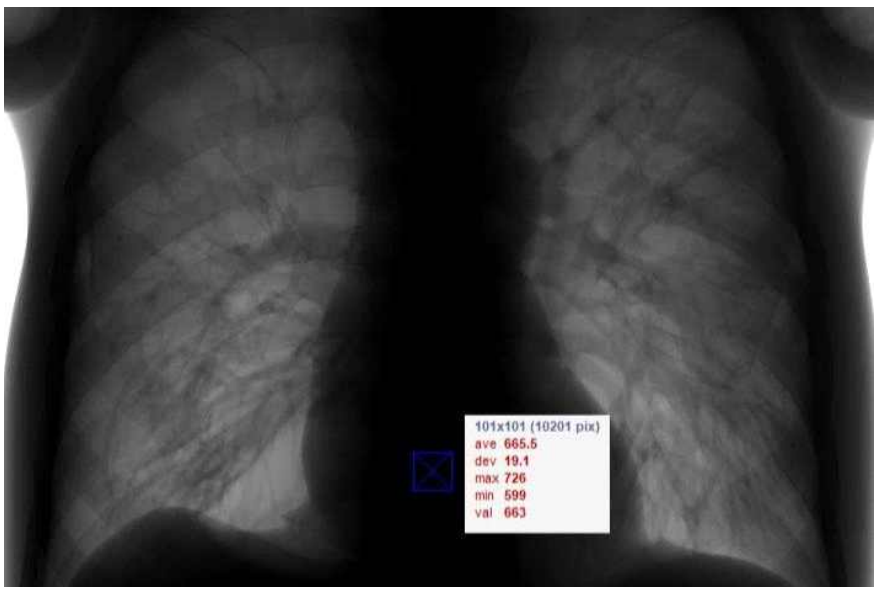

(b)

Figure 39. Chest AP raw image showing the ADU in the SiPM area (a) manufacturer's standard : 81.9 μGy (b) SiPM dose Control : 27.9 μGy

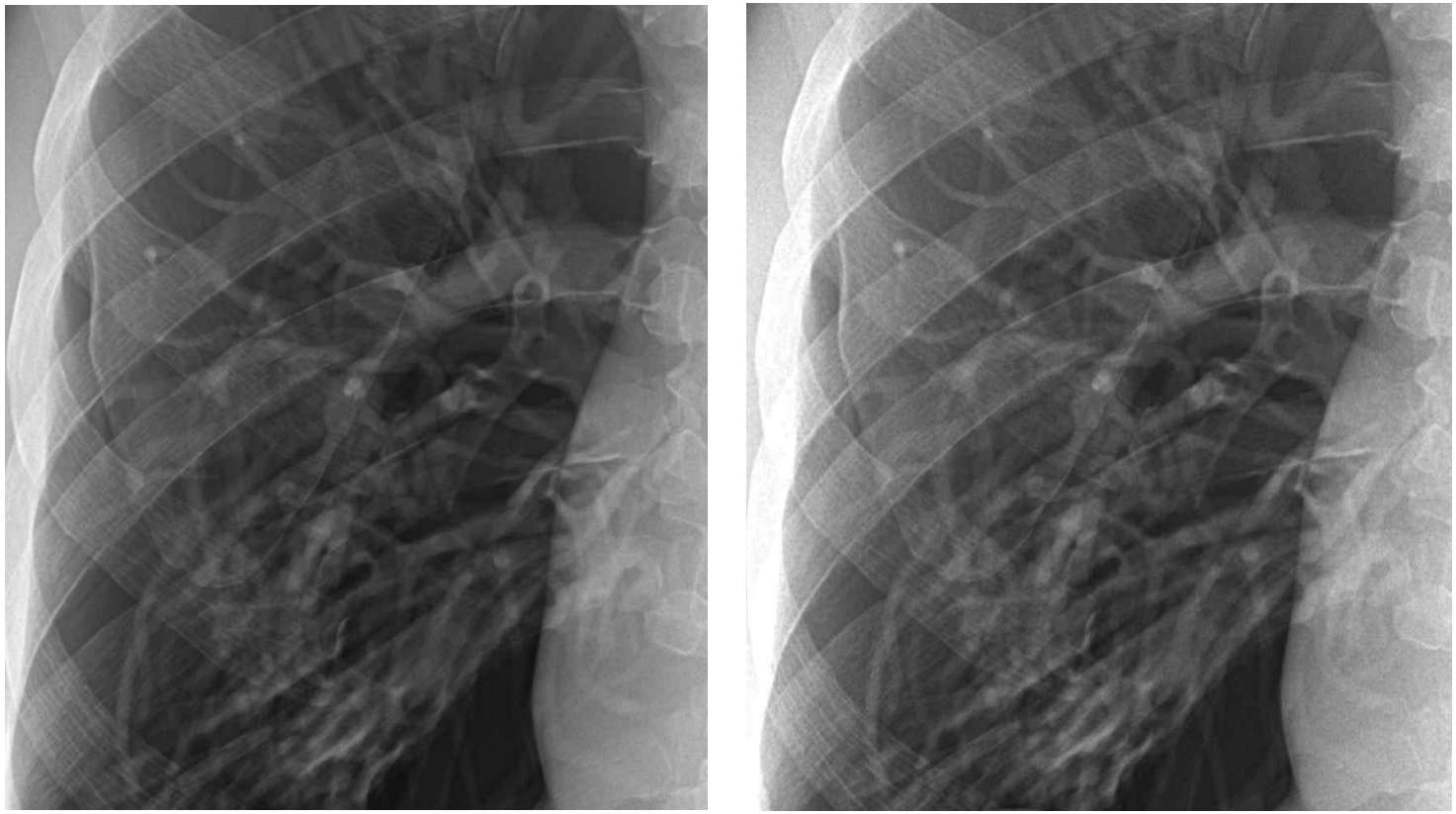

(a) (b)

Figure 40. The hilum and mediastinum for the left lung

(a) manufacturer's standard : 81.9 μGy (b) SiPM dose Control : 27.9 μGy

X-ray Image List

1. **Skull AP View**

	Manufacturer dose conditions	SiPM dose Control
Image		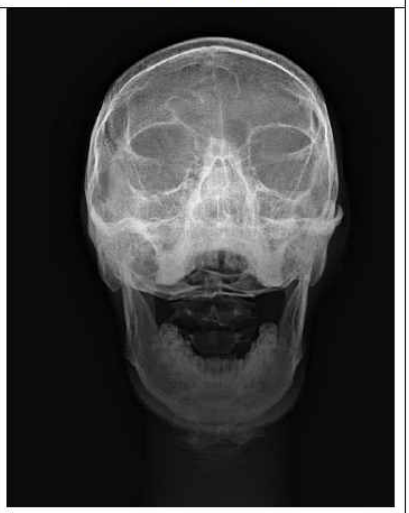
Study	Skull AP	Skull AP
Center X-ray	Nasal aperture	Nasal aperture
Date	DEC–05-2023	DEC–05-2023
Patient's inform	Skull Phantom	Skull Phantom
Magnification Rate	10.0IN X 12.0IN (Magnification Rate : 1.0)	10.0IN X 12.0IN (Magnification Rate : 1.0)
Point of view	No abnormal findings are noted in bony calvarium, orbits, craniofacial, and paranasal sinuses visualization	No abnormal findings are noted in bony calvarium, orbits, craniofacial, and paranasal sinuses visualization
Conclusion	Unremarkable findings	Unremarkable Findings
Findings	No difference in anatomical structure between dose control and manufacturer images	
Image Acquisition	Dicom3.0	Dicom3.0
Exposure Conditions	Tube Voltage: 75kV Tube Current:: 200mA Tube Current Time: 20mAs	Tube Voltage: 70kV Tube Current:: 200mA Tube Current Time: 8.87mAs

Figure 41. Image Scorecard Page 1 of 5

The imaging evaluated(**Skull AP View**) (Check Grade S,A,B,C)

Contents	Evaluate Contents		Grade	
			Manufacturer	SiPM
The status of the **permeable** Contrast and Resolution	Frontal Bone inspection	Visible Clearly	3	3
	Maxillary Bone Inspection	Visible Clearly	4	4
	Mandible Bone Inspection	Visible Clearly	4	4
	Sphenoid Bone Inspection	Visible Clearly	4	4
	Nasal cavity Inspection	Visible Clearly	3	3
	Frontal sinus Inspection	Visible Clearly	4	4
	Maxillary sinus Inspection	Visible Clearly	4	4
	Pyramid inspection	Visible Clearly	4	4
Average			3.75	3.75

(Grade S : Perfect=4 , A : excellent=3 , B : average=2 C : poor=1)

Figure 42. Image Scorecard Page 2 of 5

2. Chest P-A View

	Manufacturer dose conditions	SiPM dose Control
Image	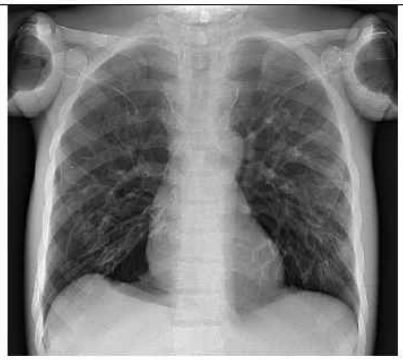	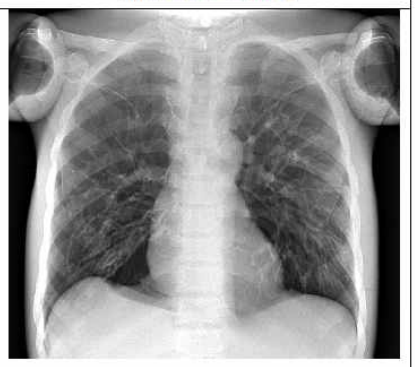
Study	Chest P-A	Chest P-A
Center X-ray	T-10 Spine	T-10 Spine
Date	DEC–05-2023	DEC–05-2023
Patient's inform	Chest Phantom	Chest Phantom
Magnification Rate	17IN X 17IN (Magnification Rate : 1.0)	17IN X 17IN (Magnification Rate : 1.0)
Point of view	No abnormal active lesions are noted in the bones of spine and chest including breastbone, ribs and collarbone. Both lungs, CP angle, and apex. Heart are unremarkable.	No abnormal active lesions are noted in the bones of spine and chest including breastbone, ribs and collarbone. Both lungs, CP angle, and apex. Heart are unremarkable
Conclusion	Unremarkable single view chest x-ray	Unremarkable single view chest x-ray
Findings	Good edge definition and grayscale of the lungs, retrocardiac & subdiaphragmatic pulmonary vessel markings, thoracic spines, and other bony chest walls. Well visualization of trachea and bronchi in mediastinum and both hila	
Image Acquisition	Dicom3.0	Dicom3.0
Exposure Conditions	Tube Voltage: 125kV Tube Current:: 200mA Tube Current Time: 2.0mAs	Tube Voltage: 125kV Tube Current:: 200mA Tube Current Time: 0.67mAs

Figure 43. Image Scorecard Page 3 of 5

The imaging evaluated(Chest P-A View) (Check Grade S,A,B,C)

Contents	Evaluate Contents		Point			
			Manufacturer		SiPM	
			UP	DN	UP	DN
The status of the permeable, Contrast and Resolution	The inspection for Lung vessel on whole of the lung field	Vessels are visible clearly on the 1/3 area of superior lung field	4	4	4	4
		Vessels are visible on 2/3 area from 1/3 area of the lung field	4	4	4	4
		Visible 1/3 of vessel only on the center of lung field	3	3	3	3
	The inspection for Lung vessel and Descending aorta in rear of heart	Visible Clearly	3	3	3	3
	Inferior diaphragm vessel Inspection	Visible Clearly	4		4	
	Rib Inspection (A costa of superior rib)	superior rib are visible clearly	4		4	
	Diaphragm Inspection	Both of side are visible clearly	4		4	
	intervertebral disc of space Inspection	Whole of intervertebral disc of space are visible clearly	4		3	
	Bronchus Inspection	Trachea, Trachea bifurcation, Principal bronchi are visible clearly	4		4	
Human work shadow	Human work shadow and undefined human work shadow	Invisible	4		4	
Average			3.71		3.64	

(Grade S : Perfect=4 , A : excellent=3 , B : average=2 C : poor=1)

Figure 44. Image Scorecard Page 4 of 5

General Review

Average value of each annotation			
No	Contents	Manufactuer	SiPM
1	Skull P-A view	3.75	3.75
2	Chest P-A view	3.71	3.69
Total Average		3.73	3.72

(Grade S : Perfect=4 , A : excellent=3 , B : average=2 C : poor=1)

Conclusion

Upon review of typical radiographs taken at the manufacturer's dose and the SiPM control showed that the SiPM in the Phantom acquisition was of similar quality for the same anatomical location at a lower dose. This can provide radiographs that are suitable for diagnostic purposes.

Figure 45. Image Scorecard Page 5 of 5

Chapter 5
Conclusion

In this paper, we present a method to realize optimal image quality and low dose control using a SiPM sensor that can be embedded in a portable X-ray detector, and verify the effectiveness through actual experiments. By evaluating the image according to the criteria of IEC62220-1, an international standard for X-ray imaging devices, we calculated the ADU value that shows optimal image performance, and implemented dose control at that ADU value through the SiPM sensor.

Evaluated by radiologists using an image scorecard, they found no clinically significant difference between cranial AP and thoracic AP images acquired with the manufacturer's reference dose and SiPM optimal dose control in identifying anatomical structures.

In the experimental results, the Skull AP was irradiated from the manufacturer's reference dose of 342.8 μGy to the optimal controlled dose of 148.3 μGy, resulting in a dose reduction of approximately 57%, and the Chest AP was irradiated from the manufacturer's reference dose of 81.9 μGy to the optimal controlled dose of 27.9 μGy, resulting in a dose reduction of 66%. These results suggest that optimal dose control with SiPM sensors can significantly reduce patient radiation exposure. However, the location of the dose detection zones is important for optimal image acquisition at the lowest dose. Typical AEC products use three to five zones, but they use large ion chamber sensors to cover a large area. SiPM, on the other hand, can be embedded in portable detectors due to its small size, but because it detects a small area, it is necessary to increase the number of sensors to detect a variety of points to overcome the limitation of the

detection area.

X-ray dose control is a very important topic in the field of medical imaging, and starting from the ALARA (As Low As Reasonably Achievable) principle introduced in the 1977 ICRP recommendation (ICRP 26), the new recommendation of ICRP publication 103 in 2008 recommends the application of the recommended dose to patients in medical radiological examinations, dose control is being carried out in advanced countries such as the United States and Europe, and the interest in dose control for patients and medical workers continues to increase in Korea [56][57]. Against this background, the experiments in this paper demonstrate that dose control for low patient exposure while maintaining optimal image quality is possible using SiPM, which is expected to make an important contribution to radiation dose management and image quality improvement in the medical imaging field.

References

[1] Young-Sub Roh, Se-Yeon Yeo, Jae-Jun Lee, Surg-Eon Sohn, "Implementation of a Full Field Digital Mammography." Journal of the Korea Academia-Industrial cooperation Society 12.10 (2011): 4578-4589.

[2] Dong-Heon Cho, "An Implementation of Radiologic Imaging Device of Remote Emergency Medical System." Journal of the Korean Institute of Illuminating and Electrical Installation Engineers 21.1 (2007): 60-65.

[3] C. Dario, A. Dunbar, F. Feliciani, M. Garcia-Barbero, "Opportunities And Challenges of E-Health and Telemedicine Via Satellite." Online Journal of Space Communication 8.14 (2021): 12.

[4] Ni. Hongyu, Chu. Jie Huang. Su, Zhou. Ji'An, Wang. Yuan, Zhu. Wenhuan, "Selecting a Suitable Portable X-ray Equipment Based on the Non-destructive Testing of Crimped Power Fittings on Transmission Lines." 2023 IEEE 3rd International Conference on Power, Electronics and Computer Applications (ICPECA). IEEE, 2023.

[5] Karim, Karim S., and Steven Tilley II. "Portable Single-Exposure Dual-Energy X-ray Detector for Improved Point-of-Care Diagnostic Imaging." Military Medicine 188.Supplement_6 (2023): 84-91.
DOI : 10.1093/milmed/usad034

[6] SONG EUN. LEE, "Impact of Radiation Technologists' Awareness and Knowledge of Medical Radiation Exposure on Safety Management Activities in University Hospitals and General Hospitals", Master of PublicHealth The Graduate School of Public Health and Welfare Konyang University, 2023

[7] Jo, Gwang-Ho, Yeong-Han Kang, Bu-Sun Kim. "A study on the exposure parameter and the patient dose for Digital Radiography system in Dae Goo." Journal of radiological science and technology 31.2 (2008): 177-182.

[8] B. K. Stewart, K. M. Kanal, J. R. Perdue, F. A. Mann, "Computed radiography dose data mining and surveillance as an ongoing quality assurance improvement process." American Journal of Roentgenology 189.1 (2007): 7-11.
DOI : 10.2214/AJR.06.1232

[9] I. A. Tsalafoutas, G. A. Blastaris, A. S. Moutsatsos, "Correlation of image quality with exposure index and processing protocol in a computed radiography system." Radiation Protection Dosimetry 130.2 (2008): 162-171.
DOI : 10.1093/rpd/ncm493

[10] W. K. Ma, P. Hogg, A. Tootell, et al. "Anthropomorphic chest phantom imaging – the potential for dose creep in computed radiography." Radiography 19.3 (2013): 207-211.
DOI : 10.1016/j.radi.2013.04.002

[11] Egbe, N. O., B. Heaton, P. F. Sharp. "Application of a simple phantom in assessing the effects of dose reduction on image quality in chest radiography." Radiography 16.2 (2010): 108-114.
DOI : 10.1016/j.radi.2009.09.007

[12] Min, H. K. "The study for performance, image quality and patient dose of various diagnostic X-ray generator." Journal of Inje University (2006): 1-101.

[13] Kwon, Hyeokjin, et al. "Usability Evaluation of Foot Pedal Switch in X-ray Radiography System." Journal of the Korean Society of Radiology 12.5 (2018): 651-658.

[14] Chang, Zeyuan, et al. "Research on X-ray Tube Characteristics Facing X-ray Fluorescence Spectrometer." 2022 Asia Communications and Photonics Conference (ACP). IEEE, 2022.
DOI : 10.1109/ACP55869.2022.10088666

[15] Santos, Luiz AP. "An overview on bipolar junction transistor as a sensor for X-ray beams used in medical diagnosis." Sensors 22.5 (2022): 1923.

[16] Lim, Jong Nam, "Photon Intensity of X-ray Tube by Voltage and Current", Doctor of Radiological Science, Graduate School of Daegu Catholic University, 2020

[17] E. Samei, Dobbins III, J. T., J. Y. Lo, M. P. Tornai, "A framework for optimizing the radiographic technique in digital X-ray imaging." Radiation Protection Dosimetry 114.1-3 (2005): 220-229.

[18] Yo Han. Chae, "Necessity of Portable X-ray Fabrication to Reduce Radiation Exposure", Master of Electronic computer engineering, The Graduate School Chonnam National University, 2021.

[19] Ishihara, K., Kato, N., Misumi, M., Kitamura, H., Hida, A., & Yamada, M. "Radiation Effects on Late-life Neurocognitive Function in Childhood Atomic Bomb Survivors: A Radiation Effects Research Foundation Adult Health Study.", Radiation Research, 197(2022), 403-407.

[20] Hess, Robert, and Ulrich Neitzel. "Optimizing image quality and dose for digital radiography of distal pediatric extremities using the contrast-to-noise ratio." RöFo-Fortschritte auf dem Gebiet der Röntgenstrahlen und der bildgebenden Verfahren. © Georg Thieme Verlag KG, 2012.

[21] P. Brosi, A. Stuessi, F. R. Verdun, P. Vock, R. Wolf, "Copper filtration in pediatric digital X-ray imaging: its impact on image quality and dose." Radiological physics and technology 4 (2011): 148-155.

[22] Bushberg, Jerrold T., and John M. Boone. The essential physics of medical imaging.

Lippincott Williams & Wilkins, 2011.

[23] Liu, Jiayin, and Jae Ho Kim. "A Novel Sub-Pixel-Shift-Based High-Resolution X-ray Flat Panel Detector." Coatings 12.7 (2022): 921.
DOI : 10.3390/coatings12070921

[24] Seibert, J. Anthony. "Flat-panel detectors: how much better are they?." Pediatric radiology 36 (2006): 173-181.
DOI : 10.1007/s00247-006-0208-0

[25] P. Eckert, H.-C. Schultz-Coulon, W. Shen, R. Stamen, and A. Tadday, "Characterization studies of silicon photomultipliers." Nuclear Instruments and Methods in Physics Research Section A: Accelerators, Spectrometers, Detectors and Associated Equipment 620.2-3 (2010): 217-226.

[26] R. G. Fardipour, M. J. Gol, M. Sahraei, M. Khakzad, "SiPM and PMT driving, signals count, and peak detection circuits, suitable for particle detection." Journal of Instrumentation 17.09 (2022): T09011.
DOI : 10.1088/1748-0221/17/09/t09011

[27] D. Grzonka, P. Bergmann, T. Hahnraths von der Gracht, P. Kulessa, W. Parol, T. Sefzick, J. Ritman, M. Zielinski, "A large area efficient trigger scintillator with SiPM read out." Nuclear Instruments and Methods in Physics Research Section A: Accelerators, Spectrometers, Detectors and Associated Equipment 1041 (2022): 167410.
DOI : 10.1016/j.nima.2022.167410

[28] Juget, Frédéric, et al. "Precise activity measurements of medical radionuclides using an ionization chamber: A case study with Terbium-161." EJNMMI physics 9.1 (2022): 19.

[29] Jin-Hyun Son, Jung-Whan Min, Hyun-soo Kim, Kwang-Yeul Lyu, Hyun-Soo Lim, Jung-Min Kim, Hoi-Woun Jeong, "Experimental study with respect to dose characteristic of glass dosimeter for low-energy by using internal detector of piranha 657." Journal of radiological science and technology 35.2 (2012): 119-124.

[30] Heydarian, M., P. W. Hoban, Alun H. Beddoe. "A comparison of dosimetry techniques in stereotactic radiosurgery." Physics in Medicine & Biology 41.1 (1996): 93.

[31] Mobit, Paul N., Alan E. Nahum, Philip Mayles. "A Monte Carlo study of the quality dependence factors of common TLD materials in photon and electron beams." Physics in Medicine & Biology 43.8 (1998): 2015.

[32] Tsuda, Masayuki. "A few remarks on photoluminescence dosimetry with high energy X-rays." Japanese Journal of Medical Physics (Igakubutsuri) 20.3 (2000): 131-139.

[33] F. Araki, T. Ikegami, T. Ishidoya, D. H. Kubo, "Measurements of Gamma Knife helmet output factors using a radiophotoluminescent glass rod dosimeter and a diode detector." Medical physics 30.8 (2003): 1976-1981.

[34] Hanjoon Yang, "A Study on the Characteristic Evaluation of Digital X-ray Imaging for CMOS Image Sensor", doctor of of Physics, Graduate School Myongji University, 2007

[35] Seungkon Han, "Study on the DQE measurement survey and the evaluation program of the X-ray detector", Master of Industrial Technology & Management, Graduate School Korea Polytechnic University, 2013

[36] J. W. Min, K. W. Kim, H. W. Jeong, "Comparison study on CNR and SNR of thoracic spine lateral radiography." Journal of radiological science and technology 36.4 (2013): 273-280.

[37] Kim, Ki-Won, et al. "Comparison study on CNR and SNR of thoracic spine lateral radiography." Journal of radiological science and technology 36.4 (2013): 273-280.

[38] https://imaging.rigaku.com/blog/how-improve-signal-noise-ration-xray-ct-images

[39] Eunae Lee, Dong Sik Kim, On the Precision of the Detective Quantum Efficiency Estimates in Digital Radiography Detectors, Journal of The Institute of Electronics and Information Engineers Vol.55, NO.5(2018): 273-280
doi : 10.5573/ieie.2018.55.5.63

[40] Kawaji, Yasuyuki, et al. "Influence of Image Resolution Property on Aliasing Error of Digital Wiener Spectrum." World Congress on Medical Physics and Biomedical Engineering 2018: June 3-8, 2018, Prague, Czech Republic (Vol. 1). Springer Singapore, 2019.

[41] Hasegawa, Akira, et al. "Noise reduction profile: A new method for evaluation of noise reduction techniques in CT." Medical physics 49.1 (2022): 186-200.

[42] Buhr, Egbert, Susanne Günther Kohfahl, and Ulrich Neitzel. "Accuracy of a simple method for deriving the presampled modulation transfer function of a digital radiographic system from an edge image." Medical physics 30.9 (2003): 2323-2331.

[43] Samei, Ehsan, Michael J. Flynn, and David A. Reimann. "A method for measuring the presampled MTF of digital radiographic systems using an edge test device." Medical physics 25.1 (1998): 102-113.

[44] T. T. Farman, R. H. Vandre, J. C. Pajak, S. R. Miller, A. Lempicki, A. G. Farman, "Effects of scintillator on the detective quantum efficiency (DQE) of a digital imaging system." Oral Surgery, Oral Medicine, Oral Pathology, Oral Radiology, and Endodontology 101.2 (2006): 219-223.

[45] N. T. Ranger, E. Samei, J. T. Dobbins III, C. E. Ravin, "Measurement of the detective quantum efficiency in digital detectors consistent with the IEC 62220 1 standard: Practical considerations regarding the choice of filter material." Medical physics 32.7Part1 (2005): 2305-2311.

[46] http://www.nmi-dr.com/#tab2

[47] Ki Hong. Kim, Study on Effects of Automatic Exposure Control for the Radiation Dose and Image Quality, Master of Electrical Engineering, Seoul National University of Technology, 2003

[48] Doyle, P., and C. J. Martin. "Calibrating automatic exposure control devices for digital radiography." Physics in Medicine & Biology 51.21 (2006): 5475.

[49] P. Doyle and C. J. Martin, "Calibrating automatic exposure control for digital radiography", physics in medicine and biology, Vol. 50, No. 21(2006), 5475 - 5485
DOI : 10.1088/0031-9155/51/21/006

[50] HAN-BYUL CHUNG. "Analysis of AEC dose according to BMI and Body size in Abdomen X-ray" master of Radiological science, Graduate School of Public Health, Eulji University, 2017

[51] Min-Gyu JEONG, "Effects of Exposure Dose Reduction by Optimization of Automatic Exposure Control Factors in Digital Radiographic Examination of Paranasal Sinus", Master of Radiological Science, Graduate School Cheongju University,2021

[52] Samei, Ehsan, Simon Murphy, Olav Christianson. "DQE of wireless digital detectors: Comparative performance with differing filtration schemes." Medical Physics 40.8 (2013): 081910.
DOI : 10.1118/1.4813298

[53] Eunae Lee, Dong Sik Kim, "On the Precision of the Detective Quantum Efficiency Estimates in Digital Radiography Detectors", Journal of The Institute of Electronics and Information Engineers Vol.55, NO.5, 2018
DOI : https://doi.org/10.5573/ieie.2018.55.5.63

[54] Coan, Paola. Development and application of the analyzer-based imaging technique with hard synchrotron radiation. Diss. European Synchrotron Radiation Facility (ESRF), 2006.

[55] Lee, Dae Hyung "NPS, MTF, DQE measurements and study of efficiency evaluation through raw data analysis of the DR detector" Master of Medical Physics, Graduate School Korea University, 2008.

[56] ICRP, 1977. Recommendations of the ICRP. ICRP Publication 26. Ann. ICRP 1 (3).

[57] Icrp. "The optimization of radiological protection: Broadening the process." Annals of the ICRP 36.3 (2006): 69-87.

Abstract in Korean

SiPM을 통한 포터블 디텍터의 피폭 선량 감소 : 최적 이미징 레벨 산출을 통한 X-ray 선량 제어 구현 및 평가

강 병 욱
생체공학 협동과정
연세대학교

휴대용 X-ray 디텍터는 소형화 및 경량화된 디자인으로 인해 환자의 위치에 빠르게 접근하여 실시간 이미지를 획득함으로써 신속하게 진단을 수행할 수 있는 장점이 있지만, 이러한 이동성 때문에 선량 제어라는 과제를 안고 있다. 본 논문에서는 휴대용 X-ray 디텍터에 내장 가능한 소형 SiPM 센서를 사용하여 최적 선량 제어를 구현함으로써 환자의 방사선 노출을 최소화하는 방법을 제시하고 그 성능을 평가하는 것을 목적으로 합니다.

이 연구에서는 엑스레이 영상장치의 국제 표준인 IEC 62220-1에 기반한 영상 평가를 통해 디텍터의 DQE와 최적의 영상 품질을 가질 수 있는 선량을 파악하고, 영상의 ADU와 SiPM 센서의 출력을 매칭하여 최적의 선량으로 제어하는 방법을 제시합니다.

실험 결과, Skull AP의 영상의 경우, 제조사 기준 선량 342.8 μGy에서 최적 제어 선량 148.3 μGy로 조사되어 약 57%의 선량 감소 효과가 확인되었다. Chest AP의 영상의 경우, 제조사 기준 81.9 μGy 대비 제어된 최적 선량 27.9 μGy로 66%의 선량 감소가 확인되었다. 이러한 결과는 SiPM 센서를 통한 최적 선량 제어가 환자의 방사선 노출을 현저히 줄일 수 있음을 입증한다.

X-선 선량 제어는 의료 영상 분야에서 매우 중요한 주제이며, 미국, 유럽 등 선진국에서는 피폭 선량 관리가 이루어지고 있으며 국내에서도 환자 및 의료 종사자의 선량 관리에 대한 연구와 관심이 계속 증가하고 있다. 이러한 배경을 통해 본 논문의 실험은 SiPM을 사용하여 최적의 이미지 품질 유지와 함께 환자의 저피폭을 위한 선량 제어가 가능함을 입증하였으며, 이는 의료 영상 분야에서의 방사선량 관리와 영상 품질 향상에 중요한 기여를 할 것으로 기대된다.

Key Words : X-ray 피폭, 최적 선량 제어, 이미지 품질, SiPM, 포터블 디텍터